

Streak instability in turbulent channel flow: the seeding mechanism of large-scale motions

Matteo de Giovanetti¹†, Hyung Jin Sung² and Yongyun Hwang¹

¹Department of Aeronautics, Imperial College London,
South Kensington SW7 2AZ, UK

²Department of Mechanical Engineering, KAIST, 291 Daehak-ro,
Yuseong-gu, Daejeon 34141, South Korea

(Received xx; revised xx; accepted xx)

It has often been proposed that the formation of large-scale motion (or bulges) is a consequence of successive mergers and/or growth of near-wall hairpin vortices. In the present study, we report our direct observation that large-scale motion is generated by an instability of an ‘amplified’ streaky motion in the outer region (i.e. very-large-scale motion). We design a numerical experiment in turbulent channel flow up to $Re_\tau \simeq 2000$ where a streamwise-uniform streaky motion is artificially driven by body forcing in the outer region computed from the previous linear theory (Hwang & Cossu, *J. Fluid Mech.*, vol. 664, 2015, pp. 51–73). As the forcing amplitude is increased, it is found that an energetic streamwise vortical structure emerges at a streamwise wavelength of $\lambda_x/h \simeq 1-5$ (h is the half-height of the channel). The application of dynamic mode decomposition and the examination of turbulence statistics reveal that this structure is a consequence of the sinuous-mode instability of the streak, a sub-process of the self-sustaining mechanism of the large-scale outer structures. It is also found that the statistical features of the vortical structure are remarkably similar to those of the large-scale motion in the outer region. Finally, it is proposed that the largest streamwise length of the streak instability determines the streamwise length scale of very-large-scale motion.

1. Introduction

Understanding the nature of coherent structures in wall-bounded turbulent shear flows has been a central research issue for many years. The near-wall region is very well understood, and contains two predominant structures: streaks (Kline *et al.* 1967; Smith & Metzler 1983) and quasi-streamwise vortices (Kim, Moin & Moser 1987; Jeong & Hussain 1997). The interplay between the two structures comprises the so-called self-sustaining process, that lies in the heart of near-wall turbulence production (Waleffe 1997; Jiménez & Pinelli 1999; Kim 2011). An important sub-process of the self-sustaining process is the ‘lift-up’ effect, by which the streamwise vortices transfer energy of the mean shear to the streaks. (Kim, Kline & Reynolds 1971; Blackwelder & Eckelmann 1979; Landahl 1980). The lift-up effect is associated with the non-normality of the linearised Navier-Stokes operator, and it is understood to play a central role in determining the spanwise spacing of the near-wall streaks (Butler & Farrell 1993; Chernyshenko & Baig 2005; del Álamo & Jiménez 2006; Pujals *et al.* 2009; Cossu *et al.* 2009; Hwang & Cossu 2010*b*; Willis *et al.* 2010). The streaks, amplified by the lift-up effect, subsequently undergo a secondary instability and/or transient growth that involves a rapid streamwise meandering motion (i.e. sinuous mode) (Hamilton, Kim & Waleffe 1995; Schoppa &

† Email address for correspondence: m.de-giovanetti14@imperial.ac.uk

Hussain 2002; Cassinelli, de Giovanetti & Hwang 2017). This is followed by the generation of vortical perturbations, which eventually develop into new streamwise vortices via non-linear mechanisms (Hamilton *et al.* 1995; Schoppa & Hussain 2002).

For the last two decades, important progress in the understanding of coherent structures in the logarithmic and outer regions has also been made. In particular, recent efforts have revealed that the ‘attached eddy hypothesis’ (Townsend 1961, 1976; Perry & Chong 1982) is the key framework for the description of the coherent structures in the logarithmic and outer regions: for instance, the logarithmic wall-normal dependence of the turbulence intensities of wall-parallel velocity components (Townsend 1976; Perry & Chong 1982; Perry & Marusic 1995; Jiménez & Hoyas 2008; Marusic *et al.* 2013), the emergence of k_x^{-1} spectra (k_x is the streamwise wavenumber) (Perry & Chong 1982; Perry *et al.* 1986; Nickels *et al.* 2005), the linear growth of the spanwise integral length scale with distance from the wall (Tomkins & Adrian 2003; Hwang & Cossu 2010*c*; Hwang 2015) and the statistical and dynamical self-similarity of coherent structures (del Álamo *et al.* 2006; Hwang & Cossu 2011; Hwang 2015; Hellström *et al.* 2016; Hwang & Bengana 2016). These findings directly support the notion that the entire logarithmic layer consists of a hierarchical form of self-similar coherent structures, as proposed in the seminal work of Townsend (1961, 1976) and Perry & Chong (1982).

A growing body of evidence further indicates that the coherent structures at a given length scale in the logarithmic and outer regions have a self-sustaining mechanism, essentially independent of those at other length scales (Hwang & Cossu 2010*c*, 2011; Hwang 2015; Hwang & Bengana 2016). Each of the self-sustaining coherent structures in the logarithmic region was found to consist of an elongated streak and streamwise vortical structures (or vortex packets), similar to that in the near-wall region (Hwang 2015). In the outer region, structures of a similar form also emerge (Hwang 2015), and it was proposed that the streak and the vortical structure correspond to very-large-scale motion (VLSM) (Kim & Adrian 1999; del Álamo & Jiménez 2003; Hutchins & Marusic 2007) and large-scale motion (LSM) (Kovaszny 1970), respectively. The self-sustaining mechanism of the structures in the logarithmic and outer regions was also found to exhibit some important similarities to that in the near-wall region (Flores & Jiménez 2010; Hwang & Bengana 2016). In particular, the generation of elongated streaks was well explained by the lift-up effect (Cossu *et al.* 2009; Pujals *et al.* 2009; Hwang & Cossu 2010*a,b*; Willis *et al.* 2010), and it was also shown that artificial inhibition of the lift-up effect destroys the self-sustaining mechanism (Hwang & Bengana 2016).

Despite this recent progress, the mechanism, by which the vortical structures in the logarithmic and outer regions are generated, remains an important issue of debate. Earlier studies proposed that mergers and/or growth of the hairpin vortices from the near-wall region could be the generation mechanism of the vortical structures in the logarithmic and outer regions (Perry *et al.* 1986; Zhou *et al.* 1999; Adrian *et al.* 2001). The largest vortical structure generated by this process was thought to be the LSM (Adrian 2007) and a VLSM was subsequently interpreted as a concatenation of adjacent LSMs (Baltzer, Adrian & Wu 2013). However, it should be pointed out that LSMs and VLSMs emerge even in the absence of motions in the near-wall and logarithmic regions (Hwang & Cossu 2010*c*; Hwang 2015). They also remain virtually unchanged in the presence of significant disruption of the near-wall region (Flores & Jiménez 2006; Hutchins & Marusic 2007). Finally, the scenario based on the mergers/growth of hairpin vortices does not provide any explanation as to why the streamwise length scale of LSMs is determined to be $\lambda_x \simeq 1 - 5\delta$ (λ_x is the streamwise wavelength, and δ is the outer length scale, such as the boundary-layer thickness, half-height of the channel, and radius of the pipe).

Unlike VLSMs which predominantly carry streamwise turbulent kinetic energy, LSMs

are the carriers of intense wall-normal and spanwise turbulent kinetic energy (Hwang 2015; Hwang & Bengana 2016). Their streamwise extent is only $O(\delta)$, considerably smaller than the $O(10\delta)$ extent of VLSMs. These features are rather similar to the near-wall streamwise vortices, the streamwise size of which is only $\lambda_x^+ \simeq 200 - 300$, compared to $\lambda_x^+ \simeq 1000$ for near-wall streaks (Jeong & Hussain 1997; Hwang 2013). This structural similarity suggests that the initiating mechanism of LSMs may be an instability of the amplified outer streak (VLSM), like that of streamwise vortices in the near-wall region. Indeed, a recent stability analysis with an eddy viscosity model revealed that the amplified streak becomes unstable at the typical streamwise length scale of LSMs and that the corresponding instability mode is characterised by a meandering motion of the streak (i.e. sinuous-mode instability) (Park *et al.* 2011; Alizard 2015).

Despite this theoretical finding, the issue of how the vortical structures in the logarithmic and outer regions are formed remains unsettled, even among the work supporting the self-sustaining process. Indeed, Jiménez (2013*a,b*) recently proposed that the Orr mechanism, which describes the transient amplification of a spanwise vortical perturbation by the mean shear, plays a role in the generation of the vortical structures. However, it should be pointed out that the Orr mechanism does not provide any description of the streamwise length-scale selection of the vortical structures, casting doubt on whether the Orr mechanism is the primary mechanism of the generation of vortical-structure. The issue of the streamwise length scale selection also appears in the recent analysis by Sharma & McKeon (2013), who investigated triadically consistent interactions between the resolvent modes. In their analysis, the length scales (wavenumbers) of the modes involved in the triadic interaction had to be ‘chosen’ from an observation of the existing database, but their analysis does not show why the system has to choose such a specific triadic interaction among many other possible combinations of the wave triad. Finally, it should be mentioned that most of the previous numerical studies have investigated the dynamics of the self-sustaining process only with a very short streamwise computational domain (Flores & Jiménez 2010; Hwang & Bengana 2016). This restriction does not allow one to explore the mechanism by which the streamwise length scale of the coherent structures at a given spanwise length scale is determined.

Given the ongoing discussion about the formation of the vortical structures in the logarithmic and outer regions, the existence of streak instability and the related streamwise length-scale selection mechanism in ‘real’ turbulent flows must be examined. In particular, this is the only scenario that provides an explanation of the streamwise length-scale selection of the vortical structures. The goal of the present study is therefore to demonstrate that the streak instability is the seeding mechanism of the vortical structure in the outer region (i.e. LSM). To this end, we design a numerical experiment that enables us to access the streak instability in a ‘real’ turbulent flow. We introduce a body forcing, computed with the previous linear theory (Hwang & Cossu 2010*b*), to drive long streaks in the outer region (i.e. an idealised form of VLSMs). The forcing amplitude is then gradually elevated to examine the emergence of streak instability and the corresponding eigenstructure. To carefully detect the eigenstructure, a dynamic mode decomposition (DMD) (Schmid 2010; Jovanović *et al.* 2014) is subsequently employed. From the designed numerical experiment, we will indeed see that sinuous-mode streak instability and the related vortical structure emerge with a streamwise length scale of $\lambda_x \simeq 1 - 5\delta$.

2. Numerical experiment

The numerical experiment in the present study has been performed in turbulent channel flow using a near-wall-resolved large-eddy simulation (LES). The streamwise,

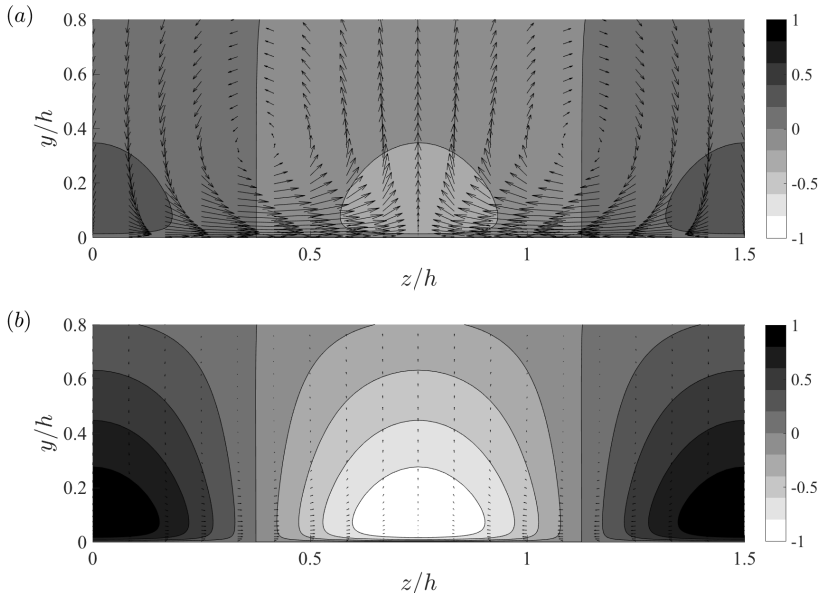


FIGURE 1. Cross-streamwise view of (a) the body forcing $\tilde{\mathbf{f}}(y, z)(= \mathbf{f})$ and (b) the response $\tilde{\mathbf{u}}(y, z)$ with (2.2). The contours indicate the streamwise component, while the vectors indicate the wall-normal and spanwise components. Here, the contour levels in (a) are normalised by the maximum value of the wall-normal component to highlight that the forcing is dominated by the cross-streamwise components (i.e. streamwise vortices), whereas those in (b) are normalised by the maximum value of the streamwise component to show that the response is dominated by the streamwise component (streak). The contours and the vectors in (a) and (b) are plotted with the same scale.

wall-normal and spanwise directions are denoted as x , y and z , respectively, and the corresponding velocities are defined as u , v and w , respectively. The lower and upper walls of the channel are set at $y = 0$ and $y = 2h$, respectively where h denotes the half-height of the channel. The numerical solver discretises the Navier-Stokes equation in the streamwise and spanwise directions using Fourier series with the $2/3$ dealiasing rule, whereas the wall-normal direction is discretised using second-order central differences. The time-stepping is performed semi-implicitly with a fractional step method: the Crank-Nicolson method is used for the terms with wall-normal derivatives and a third-order Runge-Kutta method is used for all the remaining terms. The residual stress in the present LES is approximated by an eddy-viscosity-based model proposed by Vreman (2004). The present LES has been previously validated over a range of Reynolds numbers from $Re_\tau \simeq 1000$ to $Re_\tau \simeq 4000$, as detailed in de Giovanetti *et al.* (2016). All the numerical simulations in the present study are performed by imposing constant mass flux across the channel.

2.1. The body forcing

Given the scope of the present study, the role of the body forcing is to drive a long streaky motion in the flow field. We obtain such a body forcing by following Hwang & Cossu (2010b), who computed a forcing that drives streaks in an optimal manner using a linear theory. We note that since the forcing is merely to drive the streak, other forms of the forcing can also be considered as long as they can drive a streaky motion. This issue

will be further discussed in §4.4. In this section, we briefly summarise the procedure to compute the forcing, and the reader may refer to Hwang & Cossu (2010*b*) for further details.

We start by considering the triple decomposition of a given flow field as in Reynolds & Hussain (1972):

$$\mathbf{u} = \mathbf{U}_0 + \tilde{\mathbf{u}} + \mathbf{u}', \quad (2.1)$$

where $\mathbf{u} = (u, v, w)$ is the velocity field, $\mathbf{U}_0 = (U_0(y), 0, 0)$ the mean velocity obtained by averaging in time and in two homogeneous directions, $\tilde{\mathbf{u}}$ the so-called ‘organised wave’, and \mathbf{u}' the random turbulent velocity fluctuation. If we strictly follow Reynolds & Hussain (1972), \mathbf{U}_0 is the mean velocity in the absence of the forcing and $\tilde{\mathbf{u}}$ is the motion induced by a systematically controllable external forcing (e.g. vibrating ribbon). Therefore, \mathbf{U}_0 is obtained by an experiment or a numerical simulation without any external forcing, whereas $\tilde{\mathbf{u}}$ is obtained by applying a suitable ensemble (or phase) average to the flow fields in the presence of the given forcing. For this reason, in the absence of any external forcing, $\tilde{\mathbf{u}}$ should become zero, and, in such a circumstance, (2.1) becomes identical to the standard Reynolds decomposition.

Now, we consider a deterministic body forcing $\mathbf{f} = (f_u, f_v, f_w)$ that will be used to drive a streak in the numerical simulation to be performed. We set the mean of the forcing, obtained by averaging in time and in two homogeneous directions, to be zero (see also (2.4*b*)) so that the forcing can be captured completely by the chosen ensemble average, i.e. $\mathbf{f} = \tilde{\mathbf{f}}$. If the size of \mathbf{f} is small, $\tilde{\mathbf{u}}$ also becomes small. In this case, the following linearised equation for $\tilde{\mathbf{u}}$ is obtained if an appropriate closure is provided to describe the effect of \mathbf{u}' on the evolution of $\tilde{\mathbf{u}}$ (Reynolds & Hussain 1972):

$$\nabla \cdot \tilde{\mathbf{u}} = 0, \quad (2.2a)$$

$$\frac{\partial \tilde{\mathbf{u}}}{\partial t} + (\mathbf{U}_0 \cdot \nabla) \tilde{\mathbf{u}} + (\tilde{\mathbf{u}} \cdot \nabla) \mathbf{U}_0 = -\frac{1}{\rho} \nabla \tilde{p} + \nabla \cdot [(\nu + \nu_t)(\nabla \tilde{\mathbf{u}} + \nabla \tilde{\mathbf{u}}^T)] + \tilde{\mathbf{f}}, \quad (2.2b)$$

where \tilde{p} is the pressure induced by the forcing and ν_t the eddy viscosity that models the effect of the surrounding turbulence \mathbf{u}' on $\tilde{\mathbf{u}}$. As in previous studies (e.g. Reynolds & Tiederman 1967), the well-known Cess model is considered for ν_t :

$$\nu_t(\eta) = \frac{\nu}{2} \left\{ 1 + \frac{\kappa^2 Re_\tau^2}{9} (1 - \eta^2)^2 (1 + 2\eta^2)^2 \times 1 - e^{[(|\eta|-1)Re_\tau/A]^2} \right\}^{\frac{1}{2}} - \frac{\nu}{2}, \quad (2.3)$$

where $\eta = (y - 1)/h$, $\kappa = 0.426$ and $A = 25.4$ from del Álamo & Jiménez (2006). The mean-velocity profile $U_0(y)$ is subsequently obtained by applying Prandtl’s mixing length model to (2.3): $\nu_t dU_0/dy = -\overline{u'v'}$ where the overbar denotes average in time and homogeneous directions. For further details on the profiles of $\nu_t(y)$ and $U_0(y)$, the reader may refer to del Álamo & Jiménez (2006) and Pujals *et al.* (2009).

The body forcing that yields the largest response of (2.2) has been previously computed in Hwang & Cossu (2010*b*). This forcing is given in the form of a counter-rotating vortical motion and it creates a streak by optimally utilising the lift-up effect (see also figure 1). Here, we compute this forcing to drive a streak in the simulation. Given the spatial homogeneity of the mean flow and the eddy viscosity in the streamwise and the spanwise directions, the solution of (2.2) is written as

$$\tilde{\mathbf{u}}(x, y, z, t) = \hat{\mathbf{u}}(y, t; k_x, k_z) e^{i(k_x x + k_z z)}, \quad (2.4a)$$

where k_x and k_z are the streamwise and spanwise wavenumbers, respectively. The body

forcing is also written in the form of

$$\tilde{\mathbf{f}}(x, y, z, t) = \hat{\mathbf{f}}(y, t; k_x, k_z) e^{i(k_x x + k_z z)}. \quad (2.4b)$$

We now assume that the forcing is harmonic in time with a prescribed real frequency ω_f , i.e. $\hat{\mathbf{f}}(y, t) = \hat{\mathbf{f}}_w(y) e^{i\omega_f t}$. Since (2.2) is a linear time-invariant system, its solution becomes $\hat{\mathbf{u}}(y, t) = \hat{\mathbf{u}}_w(y) e^{i\omega_f t}$ after initial transience. Then, the forcing profile leading to the largest response will be computed by solving the following optimisation problem:

$$\max_{\omega_f} \max_{\|\hat{\mathbf{f}}_w\| \neq 0} \frac{\|\hat{\mathbf{u}}_w\|}{\|\hat{\mathbf{f}}_w\|}, \quad (2.5)$$

where $\|\cdot\|^2 \equiv (1/h) \int_{-h}^h (\cdot)^H (\cdot) dy$ and $(\cdot)^H$ indicates the complex conjugate transpose.

The solution procedure of (2.5) typically involves the computation of the 2-norm of the so-called resolvent operator (Schmid & Henningson 2001). In this study, the optimisation problem (2.5) is solved by repeating the calculation by Hwang & Cossu (2010b) using their numerical solver with the same wall-normal resolution. Since the present study is concerned with the instability of the streak at large scales (i.e. VLSM), the spanwise spacing of the forcing needs to be identical to that of VLSM. Since the mean spanwise spacing of the VLSM in turbulent channel flow was found to be $\lambda_z \simeq 1.5h$ (del Álamo & Jiménez 2003; Hwang 2015), the spanwise wavenumber of the forcing is chosen to be $k_z = 2\pi/1.5h$. To generate the streamwise-uniform streaky mean flow, the streamwise wavenumber and the forcing frequency are chosen to be $k_x = 0$ and $\omega_f = 0$, respectively. We note that, for a given spanwise wavenumber k_z , this choice of k_x and ω_f yields the largest response of $\tilde{\mathbf{u}}$ with (2.2) (see below for further explanation). Also, the streamwise-uniform streaky mean flow allows us to examine all possible streamwise wavelengths of the streak instability.

Fig. 1 shows the cross-streamwise view of the computed optimal forcing profile $\tilde{\mathbf{f}}$ and the corresponding response $\tilde{\mathbf{u}}$ of (2.2). The forcing \mathbf{f} is given in the form of a pair of counter-rotating streamwise vortices, and is dominated by the cross-streamwise velocity components (figure 1a). On the other hand, the response velocity field $\tilde{\mathbf{u}}$ is dominated by a streaky motion of the streamwise velocity and its cross-streamwise velocity components are much weaker than the streamwise one (figure 1b). This indicates that the cross-streamwise components in the forcing are used to amplify the streamwise velocity streak in the response field. This is the so-called ‘lift-up’ effect, in which the streamwise velocity component is highly amplified by the presence of a small amount of the cross-streamwise velocity components (the wall-normal one in particular).

The lift-up effect can be better understood from the wall-normal velocity and vorticity form of the linearised equation for $\hat{\mathbf{u}}(y, t; k_x, k_z)$: i.e.

$$\begin{aligned} \frac{\partial}{\partial t} \begin{bmatrix} \hat{v} \\ \hat{\omega}_y \end{bmatrix} &= \begin{bmatrix} \Delta^{-1} \mathcal{L}_{OS} & 0 \\ -ik_z U' & \mathcal{L}_{SQ} \end{bmatrix} \begin{bmatrix} \hat{v} \\ \hat{\omega}_y \end{bmatrix} \\ &+ \begin{bmatrix} -ik_x \Delta^{-1} \mathcal{D} & -k^2 \Delta^{-1} & -ik_z \Delta^{-1} \mathcal{D} \\ ik_z & 0 & -ik_x \end{bmatrix} \begin{bmatrix} \hat{f}_x \\ \hat{f}_y \\ \hat{f}_z \end{bmatrix}, \end{aligned} \quad (2.6a)$$

where

$$\mathcal{L}_{OS} = -ik_x (U \Delta - U'') + \nu_T \Delta^2 + 2\nu_T' \Delta \mathcal{D} + \nu_T'' (\mathcal{D}^2 + k^2), \quad (2.6b)$$

$$\mathcal{L}_{SQ} = -ik_x U + \nu_T \Delta + \nu_T' \mathcal{D}. \quad (2.6c)$$

Here, $\hat{\omega}_y$ is the wall-normal vorticity of $\hat{\mathbf{u}}(y, t; k_x, k_z)$, $\nu_T = \nu + \nu_t$, $\Delta = \mathcal{D}^2 - k^2$, $k^2 =$

$k_x^2 + k_z^2$, and \mathcal{D} and $'$ denote $\partial/\partial y$. In (2.6), it is important to note that the equation for $\hat{\omega}_y$ (the Squire equation) is passively coupled with the equation for \hat{v} (the Orr-Sommerfeld equation) via the off-diagonal term $-ik_z U'$. Therefore, the energy transfer between the wall-normal velocity and vorticity in (2.6) should always take place from \hat{v} to $\hat{\omega}_y$ (Schmid & Henningson 2001). Furthermore, it should be noted that, for given \hat{v} , the amplification of $\hat{\omega}_y$ is solely governed by the Squire equation. Therefore, the largest amplification by the optimal forcing is expected in the set of streamwise and spanwise wavenumbers which would minimise the effect of dissipation in the Squire equation, while maximising the role of its driving term. In the Squire equation, the effect of dissipation is roughly proportional to $k^2 (= k_x^2 + k_z^2)$, whereas the driving term is only proportional to k_z . Therefore, the largest possible amplification by the forcing is expected at $k_x = 0$ and $k_z \simeq O(U'l/\nu_T)$ with l being the length scale of ω_y , as also confirmed by numerous previous studies (e.g. Schmid & Henningson 2001). In this case, the main energy transfer between the velocity components of the linearised Navier-Stokes equation should be from \hat{v} to \hat{u} . This is also why the optimal forcing is featured by large cross-streamwise components and its response is dominated by a large streamwise component (see figure 1).

Finally, it is important to mention that the linearised equation (2.6) does not allow for any mechanism of energy transfer from $\hat{\omega}_y$ (i.e. \hat{u} and \hat{w}) to \hat{v} because the equation for \hat{v} is independent of $\hat{\omega}_y$. Such a mechanism is only achieved through the nonlinearity of the Navier-Stokes equation. Therefore, describing the dynamics of the wall-normal velocity with any kind of linear theory would be physically unmeaningful and incomplete. We will see that the streak instability mechanism provides a sound explanation for the generation of the wall-normal velocity from the highly amplified streamwise velocity structure (i.e. streak). In this respect, it is also worth mentioning that studying the streak instability mechanism would provide physical insight into design of constant or dynamical modifications of the linearized Navier-Stokes equations around turbulent mean velocity. Therefore, this effect may be modelled by various forms of deterministic and stochastic forcing introduced into the linearized dynamics, as also recently shown by Zare *et al.* (2017).

2.2. Dynamic mode decomposition

Dynamic mode decomposition (DMD) (e.g. Schmid 2010) is employed to detect the eigenstructure of the streak instability using a set of flow-field snapshots detailed in §3.3. The DMD is an increasingly popular post-processing technique for analysis of the temporal and spatial evolution of given flow structures of interest. It approximates the flow-field evolution with a finite-dimensional linear time-invariant (LTI) dynamical system. The DMD employed in the present study follows the one proposed by Jovanović, Schmid & Nichols (2014) and, here, we only provide a brief summary of their approach.

We consider a sequence of equally time-spaced complex-valued snapshots with a time interval Δt , such that $\psi_n \equiv \psi(n\Delta t)$ where ψ_n is the flow field at $t = n\Delta t$ for $n = 0, 1, 2, \dots, N$. If the temporal evolution of the given flow field is assumed to be generated by a discrete-time LTI system, it can be written as

$$\psi_{n+1} = \mathbf{A}\psi_n. \quad (2.7)$$

The snapshots, each composed of M spatial points, are then collected in two ordered matrices Ψ_0 and Ψ_1 , such that

$$\Psi_0 = [\psi_0, \psi_1, \psi_2, \dots, \psi_{N-1}] \in \mathbb{C}^{M \times N}, \quad (2.8a)$$

$$\Psi_1 = [\psi_1, \psi_2, \psi_3, \dots, \psi_N] \in \mathbb{C}^{M \times N}. \quad (2.8b)$$

<i>Case</i>	Re_m	Re_τ	L_x/h	L_z/h	$N_x \times N_y \times N_z$	Δx^+	Δz^+	Δy_1^+
S490	17800	494	25.0	3.0	$288 \times 81 \times 72$	64.7	32.3	1.45
S960	38100	960	25.0	3.0	$576 \times 81 \times 144$	62.5	33.4	1.80
S2050	89100	2056	12.0	3.0	$576 \times 129 \times 288$	64.3	32.1	1.44

TABLE 1. Simulation parameters of the unforced cases (before dealiasing).

The relation between Ψ_0 and Ψ_1 is subsequently given by

$$\Psi_1 = \mathbf{A}\Psi_0. \quad (2.9)$$

Here, the matrix \mathbf{A} may be a suitable approximation of the so-called Koopman operator, especially when the snapshots are collected from a statistically stationary flow. A DMD is essentially an algorithm that computes eigenvalues and the corresponding eigenmodes (dynamic modes) of \mathbf{A} only using the snapshots ψ_n .

The approximation of \mathbf{A} in this study is made by combining with POD (proper orthogonal decomposition). This approach enables us to robustly implement the DMD, as it prevents mathematically singular construction of the companion matrix of \mathbf{A} from noise and other uncertainties in the snapshots (e.g. small-scale background turbulence in the present study) (Schmid 2010). The POD is performed with an economy-size singular value decomposition of the snapshot matrix Ψ_0 , i.e. $\Psi_0 = \mathbf{U}\Sigma\mathbf{V}^H$, where $\Sigma = \text{diag}\{\sigma_1, \sigma_2, \dots, \sigma_{N_p}\}$ with non-zero real positive singular value σ_m for $m = 1, 2, \dots, N_p$ ($N_p \leq N$), and $\mathbf{U} \in \mathbb{C}^{M \times N_p}$ and $\mathbf{V} \in \mathbb{C}^{N \times N_p}$ are unitary matrices. Each POD mode is then given by the m -th column vector of \mathbf{U} with the corresponding energy σ_m , and its temporal dynamics are described by the m -th column vector of \mathbf{V} . Here, if one is to use only the first r POD modes ($r \leq N_p$), $\Psi_0 \simeq \mathbf{U}_r \Sigma_r \mathbf{V}_r^H$ where $\Sigma_r = \text{diag}\{\sigma_1, \sigma_2, \dots, \sigma_r\}$, $\mathbf{U}_r \in \mathbb{C}^{M \times r}$ and $\mathbf{V}_r \in \mathbb{C}^{N \times r}$.

Projection of \mathbf{A} onto the subspace of the first r POD modes is then given by

$$\mathbf{S} = \mathbf{U}_r^H \mathbf{A} \mathbf{U}_r = \mathbf{U}_r^H \Psi_1 \mathbf{V}_r \Sigma_r^{-1}, \quad (2.10)$$

where $\mathbf{S} \in \mathbb{C}^{r \times r}$. The eigenvalues of \mathbf{S} , denoted by μ_j , then approximate some of the leading eigenvalues of \mathbf{A} and the corresponding eigenvectors \mathbf{y}_j construct the dynamic modes from

$$\phi_j = \mathbf{U}_r \mathbf{y}_j. \quad (2.11)$$

Any snapshot may then be expressed in terms of a series expansion of the dynamic modes, such that:

$$\psi_n \simeq \sum_{j=1}^r \alpha_j \mu_j^n \phi_j, \quad (2.12)$$

where α_j is the amplitude of each dynamic mode ϕ_j , which represents its relative contribution. In this study, α_j has been calculated following the standard (non-sparsity-promoting) optimisation procedure in Jovanović *et al.* (2014).

3. Results

The designed experiment is carried out with a set of numerical simulations documented in table 1. Three different Reynolds numbers are considered, but most of the data presented in this section will be from the numerical simulations at $Re_\tau \simeq 960$ (S960).

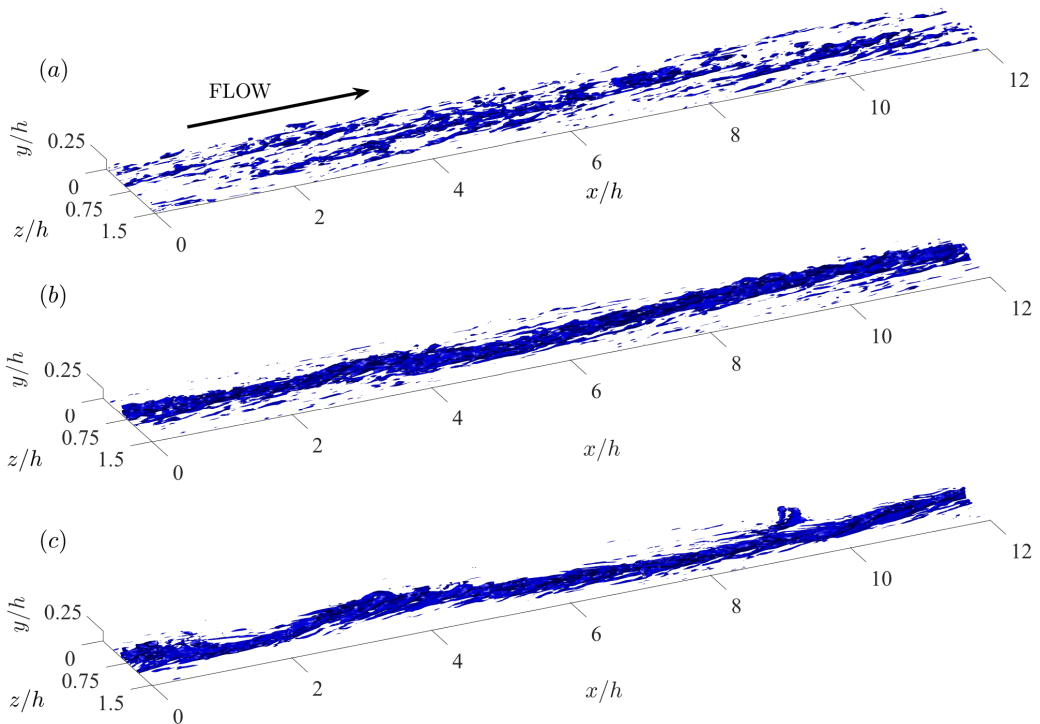


FIGURE 2. Iso-surfaces of instantaneous streamwise velocity ($u'^+ = -3.5$) for S960: (a) $\|\mathbf{f}h/u_{\tau,\text{ref}}^2\| = 0.31$ ($A_s^+ = 1.44$), (b) $\|\mathbf{f}h/u_{\tau,\text{ref}}^2\| = 0.94$ ($A_s^+ = 3.42$), (c) $\|\mathbf{f}h/u_{\tau,\text{ref}}^2\| = 6.11$ ($A_s^+ = 5.30$).

However, we note that the findings at this Reynolds number are qualitatively the same as those at the other two Reynolds numbers (see e.g. §3.3). The body forcing computed in §2.1 is implemented in each of the numerical simulations and the forcing amplitude is gradually increased to drive stronger streaks. The forcing amplitude is defined as

$$\|\mathbf{f}\| = \sqrt{\frac{2}{V} \int_V \mathbf{f}^H \mathbf{f} dV}, \quad (3.1)$$

where V is the total volume of the computational domain. We note that the factor 2 is introduced here to make the norm in (3.1) identical to the one in (2.5) and that $\mathbf{f} = \tilde{\mathbf{f}}$ by the definition of the forcing introduced in §2.1.

Application of the forcing is found to affect friction drag and the related Re_τ . However, for all forcing amplitudes considered, there was no case resulting in any drag reduction, consistent with the recent work by Canton *et al.* (2016). For small forcing amplitudes, the friction Reynolds number Re_τ of the simulations changes very little. However, as the forcing amplitude is increased further, Re_τ increases significantly: see table 2 for the case of the S960 simulations. Here, it should be noted that the elevated skin friction is not due to any interaction with structures at smaller length scales in the near-wall and logarithmic regions. In fact, the introduction of the large-amplitude forcing has been found to destroy a significant amount of the structures in these regions (see figure 6). Instead, the increase in skin friction for such large forcing amplitudes appears to be due to direct effect of the forcing on the wall shear stress. This interpretation is consistent

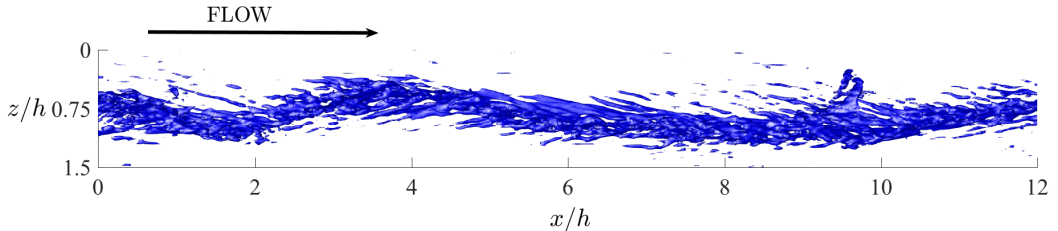


FIGURE 3. Top view of the iso-surfaces of instantaneous streamwise velocity ($u'^+ = -3.5$) in figure 2 (c). Here, the flow direction is from left to right.

$\ \mathbf{f}h/u_{\tau,\text{ref}}^2\ $	0	0.11	0.31	0.68	0.94	1.90	3.85	6.11	8.06
Re_τ	960	967	992	1021	1029	1034	1042	1078	1121
$\ \tilde{\mathbf{u}}_s^+\ $	0	0.63	1.90	2.53	2.76	3.00	3.42	3.79	4.04
A_s^+	0	0.54	1.44	2.96	3.42	4.04	4.73	5.30	5.72

TABLE 2. Summary of flow response with respect to the forcing amplitude (S960).

with our recent findings (Hwang & Bengana 2016; de Giovanetti *et al.* 2016) where the lift-up effect was found to be an important skin-friction generation mechanism of the structures in the logarithmic and outer regions. Indeed, the forcing in the present study, given in the form of counter-rotating vortices (figure 1), is designed to generate a streak by promoting the lift-up effect.

It should finally be mentioned that the main focus of the present study is the comparison of the reference and forced simulations in order to identify the flow structures associated with streak instability statistically and dynamically. Therefore, all data from the forced simulations are presented by scaling with the friction velocity of the (unforced) reference simulations, $u_{\tau,\text{ref}}$.

3.1. Streak amplification

Figure 2 reports the instantaneous streamwise velocity fluctuation of case S960 on increasing the forcing amplitude. Given the spanwise wavelength of the forcing ($\lambda_z/h = 1.5$), two streaks are driven in our computational domain (see table 1). Here, for brevity, we only present half of the spanwise domain. As the forcing amplitude is gradually increased (from figure 2a to c), a streaky structure covering the entire streamwise domain clearly emerges. It is also interesting to note that the highly amplified streak appears to meander along the streamwise direction (figure 2c) and this is clearly seen in figure 3, where a top view of figure 2 (c) is given. This meandering behaviour of the driven streak is reminiscent of that reported for VLSMs in a turbulent boundary layer (Hutchins & Marusic 2007). However, more quantitative discussion of this feature will be deferred to §3.2 and §3.3.

The streaky structure driven by the body forcing in the numerical simulations is detected statistically using the definition of the triple decomposition in (2.1). Since the applied body forcing is steady and uniform in the streamwise direction, it is evident that the ensemble average in (2.1) is replaced by the average in time and the streamwise

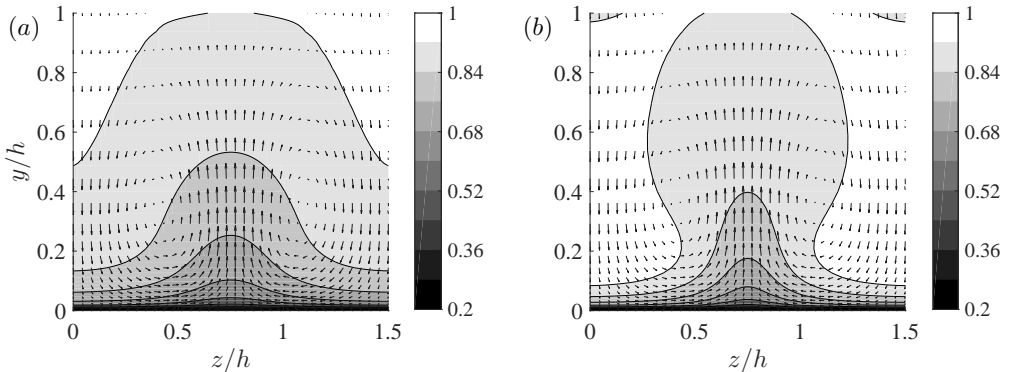


FIGURE 4. Mean cross-stream flow field for S960: (a) $\|\mathbf{f}h/u_{\tau,\text{ref}}^2\| = 0.31$ ($A_s^+ = 1.44$); (b) $\|\mathbf{f}h/u_{\tau,\text{ref}}^2\| = 1.90$ ($A_s^+ = 4.04$). The contours indicate the streamwise velocity, and the arrows represent the wall-normal and spanwise velocities. The contours are normalised by the centreline velocity of each simulation.

direction. The organised wave in a simulation with the forcing is then obtained by

$$\tilde{\mathbf{u}}_s = \langle \mathbf{u} - \mathbf{U}_0 \rangle_{x,t}, \quad (3.2)$$

where the subscript ‘ s ’ on the left-hand side denotes the organised wave component obtained by a numerical simulation and $\langle \cdot \rangle_{x,t}$ indicates the average in time and in the streamwise direction. We also recall that $\mathbf{U}_0 = (U_0(y), 0, 0)$ is the mean velocity of the reference (unforced) simulation.

The cross-streamwise view of the mean velocity ($\langle \mathbf{u} \rangle_{x,t} = \mathbf{U}_0 + \tilde{\mathbf{u}}_s$) is shown in figure 4 for two different forcing amplitudes. The appearance of a low-velocity region is evident around $z/h = 0.75$, where the streamwise momentum is expected to be pumped away from the wall by the counter-rotating vortical forcing (see also figure 1). The low-speed region extends along the entire wall-normal location including the logarithmic layer ($0.05 < y/h < 0.2$ at this Reynolds number). Two symmetric high-velocity regions arise both sides of the low-velocity region, where the streamwise momentum is supposed to be brought down to the wall by the forcing. An increase in the forcing amplitude results in the narrower spanwise extent of the low-speed region (compare figure 4a with 4b), as was also reported for the near-wall case (Cassinelli *et al.* 2017). Finally, it should be mentioned that $\tilde{\mathbf{u}}_s$ is dominated by the streamwise velocity: for example, when $\|\mathbf{f}h/u_{\tau,\text{ref}}^2\| = 1.91$, the maximum streamwise component of $\tilde{\mathbf{u}}_s$ is $\tilde{u}_{s,\text{max}}^+ = 4.76$, while its wall-normal counterpart is only $\tilde{v}_{s,\text{max}}^+ = 1.01$ (the superscript ‘+’ denotes scaling in the inner units). This indicates that the formation of the streaky mean flow is a consequence of the lift-up effect, as explained in detail in §2.1.

Using the computed $\tilde{\mathbf{u}}_s$, two quantities are computed to measure the response to the forcing. The first one is the norm of $\tilde{\mathbf{u}}_s$:

$$\|\tilde{\mathbf{u}}_s\| = \sqrt{\frac{2}{V} \int_V \tilde{\mathbf{u}}_s^H \tilde{\mathbf{u}}_s dV}, \quad (3.3)$$

which represents the kinetic energy of the induced motion averaged over the given computational domain. We note that if the forcing amplitude is small and the eddy viscosity in (2.3) correctly models the surrounding turbulence, $\tilde{\mathbf{u}}_s$ from (3.2) would be identical to $\tilde{\mathbf{u}}$ from the linear model (2.2). Although, in practice, this is unlikely to happen due to the crude nature of the eddy-viscosity model, computation of $\|\tilde{\mathbf{u}}_s\|$ as in (3.3)

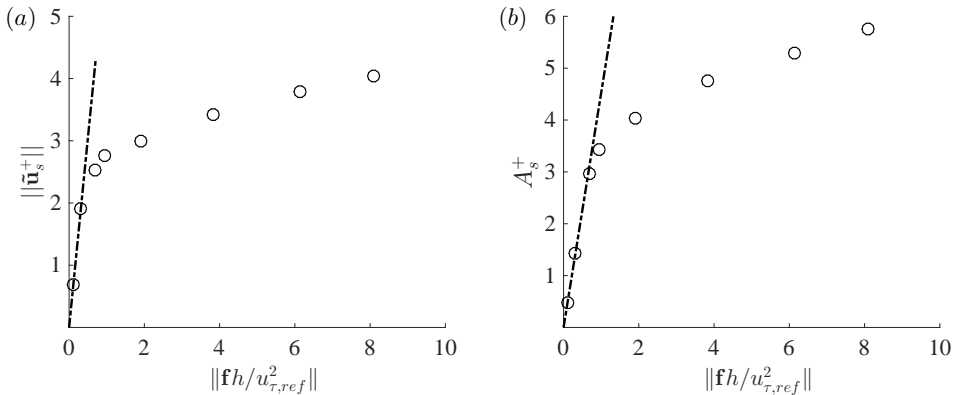


FIGURE 5. Flow response to the forcing for S960: (a) $\|\tilde{\mathbf{u}}_s^+\|$; (b) A_s^+ . Here, the definitions of $\|\tilde{\mathbf{u}}_s^+\|$ and A_s^+ are given in (3.3) and (3.4), respectively.

would be useful to assess the linear model (2.2), enabling the quantitative comparison of the amplification by the forcing in a real turbulent flow with that in the linear model (2.2). The second measure of the response to the forcing is chosen to be the streak amplitude and is defined as

$$A_s^+ = \frac{1}{2} \left(\max_{y,z} [\tilde{u}_s^+(y,z)] - \min_{y,z} [\tilde{u}_s^+(y,z)] \right), \quad (3.4)$$

where \tilde{u}_s^+ is the streamwise component of $\tilde{\mathbf{u}}_s$. This definition follows that used in a laminar boundary layer and previous studies (Andersson *et al.* 2001; Park *et al.* 2011; Alizard 2015; Cassinelli *et al.* 2017).

The evolution of the two quantities on increasing the forcing amplitude is shown in figure 5. As expected, both $\|\tilde{\mathbf{u}}_s^+\|$ and A_s^+ increase linearly with $\|\mathbf{f}\|$ at small forcing amplitudes (i.e. $\|\mathbf{f}h/u_{\tau,\text{ref}}^2\| \lesssim 0.5$). The linear fit is found to follow $\|\tilde{\mathbf{u}}_s^+\|/\|\mathbf{f}h/u_{\tau,\text{ref}}^2\| \simeq 6.2$. This value is fairly close to $\|\tilde{\mathbf{u}}^+\|/\|\tilde{\mathbf{f}}h/u_{\tau}^2\| = 4.0$ obtained with the linear theory based on (2.2) (note that $\mathbf{f} = \tilde{\mathbf{f}}$), suggesting that the eddy viscosity in (2.3) is reasonably a good approximation (see also §4.4). When the forcing amplitude is large enough, neither $\|\tilde{\mathbf{u}}_s^+\|$ nor A_s^+ increase linearly anymore, showing a nonlinear behaviour. The largest forcing amplitude considered for the S960 case is $\|\mathbf{f}h/u_{\tau,\text{ref}}^2\| = 8.09$. However, as we shall see in §4.1, this forcing amplitude is too high to study the physical processes in a natural unforced flow. Therefore, forcing amplitude greater than this value is not considered.

3.2. Streak instability: spectra and rms

Now, we investigate the emergence of other flow structures from the driven streamwise-uniform streaks. The focus of this section is given to the detection of wall-normal and spanwise velocity fluctuations at $1 < \lambda_x/h < 5$, as this is the main statistical feature of LSMs (Hwang 2015). All velocity spectra analyzed in this section have been normalized using the friction velocity of the reference (unforced) simulation. Fig. 6 shows the evolution of the streamwise wavenumber spectra of the wall-normal velocity, as the streak (and forcing) amplitude is increased. In the absence of any forcing (figure 6a), the spectra are well aligned along the linear ridge $y = 0.35\lambda_x$, as pointed out by Hwang (2015). At the top end of the linear edge (i.e. $y/h \geq 0.4 - 0.6$), the spectra show their peak at $\lambda_x/h \simeq 1 - 2$, as in other direct numerical simulations (e.g. Hoyas & Jiménez 2006). Although this streamwise wavelength is a little shorter than $\lambda_x/h \simeq 3 - 4$ observed in the streamwise velocity spectra (Monty *et al.* 2009), it is evident that this part

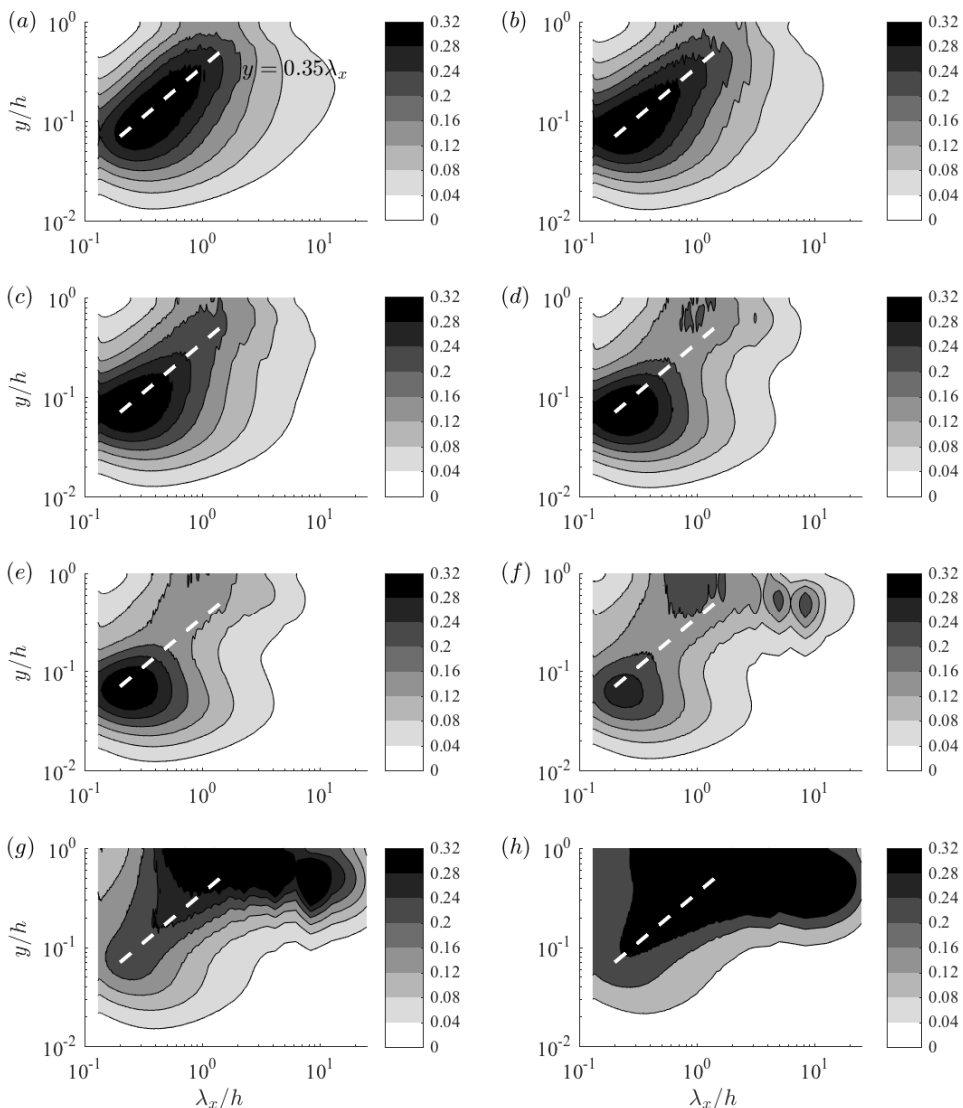


FIGURE 6. Premultiplied streamwise wavenumber spectra of wall-normal velocity (S960). (a) $A_s^+ = 0$ (unforced); (b) $A_s^+ = 0.54$; (c) $A_s^+ = 1.44$; (d) $A_s^+ = 2.96$; (e) $A_s^+ = 3.42$; (f) $A_s^+ = 4.04$; (g) $A_s^+ = 4.76$; (h) $A_s^+ = 5.30$. Here, the thick white dashed line indicates $y = 0.35\lambda_x$.

would correspond to LSMs, given its wall-normal location and streamwise wavelength. Application of the forcing is found to significantly change the wall-normal velocity spectra. Even at fairly small forcing amplitudes (figures 6b, c), the spectral intensity around the channel centre for $\lambda_x/h \simeq 1 - 2$ is slightly elevated compared to the unforced case (figure 6a). As the forcing amplitude is further increased, the spectra reveal a well-manifested peak at $\lambda_x/h \simeq 1 - 2h$ and $y/h \geq 0.4 - 0.6$, consistent with the location of LSMs (figures 6d, e). At excessively large forcing amplitudes (figures 6f-h), excitation at larger streamwise length scales is observed. However, the excited streamwise wavelength does not exceed $\lambda_x/h \simeq 10$ at least for $A_s^+ < 5$ (figure 6g).

Through the elevation of the forcing amplitude, it has been consistently observed that

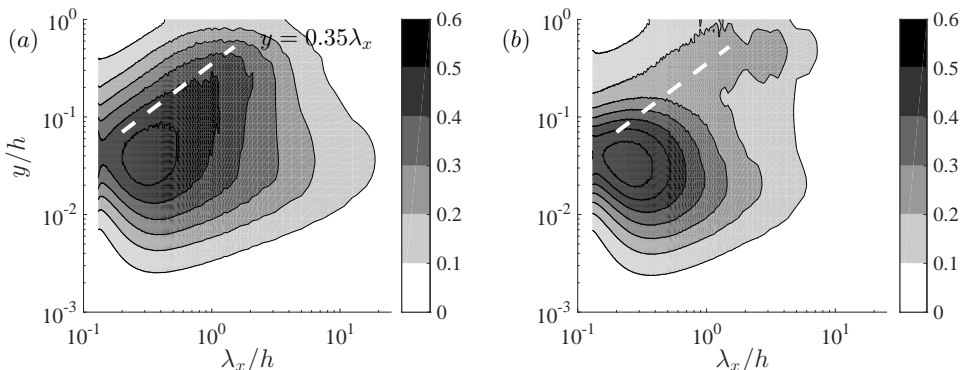


FIGURE 7. Premultiplied streamwise wavenumber spectra of spanwise velocity (S960): (a) $A_s^+ = 0$ (unforced); (b) $A_s^+ = 3.42$. Here, the thick white dashed line indicates $y = 0.35\lambda_x$.

the forcing significantly affects the structures at smaller length scales in the near-wall and logarithmic regions. Indeed, the increase in the forcing amplitude gradually reduces the activity in the logarithmic region (figures 6*b-e*), significantly weakening even the near-wall processes eventually (figures 6*f-h*). It is not clear yet why the application of such a body forcing significantly inhibits the processes at smaller scales in the near-wall and logarithmic regions. However, this feature reminds us of the suppression of the near-wall process, previously observed when a large-scale counter-rotating vortical body forcing is applied at low Reynolds numbers (Schoppa & Hussain 1998; Willis *et al.* 2010; Canton *et al.* 2016). Indeed, the inhibition of the structures at smaller scales in figure 6 is consistent with previous observations. However, in the present study, the suppression of the near-wall and logarithmic regions did not yield any skin-friction reduction, unlike previous studies at low Reynolds numbers. This is because the forcing itself has elevated the skin-friction generation process at the scale of the applied forcing via the enhanced lift-up effect (see also the discussion in §3.1). Finally, we note that the observed suppression of the processes at smaller scales is clearly due to an interaction of the forcing with other scales. Therefore, further discussion on this issue is beyond the scope of the present study.

The behaviour of the spanwise velocity spectra on increasing the forcing amplitude has also been found to be qualitatively the same as that of the wall-normal velocity spectra. Fig. 7 shows the streamwise wavenumber spectra of the spanwise velocity for the unforced and forced cases. Similar to the wall-normal velocity spectra, the forcing resulting in $A_s^+ \simeq 3-4$ excites the spectral intensity at $\lambda_x/h \simeq 1-2$ and $y/h \geq 0.4-0.6$, while weakening the activity of the structures in the near-wall and logarithmic regions.

The observation made with figures 6 and 7 suggests that an intense cross-streamwise velocity structure at $\lambda_x/h \simeq 1-2$ is excited at low amplitudes of the body forcing. It is important to remember that the applied forcing is uniform in the streamwise direction ($\lambda_x = \infty$), thus this cross-streamwise velocity structure at a finite streamwise length scale should not be the direct outcome of the forcing. Instead, it suggests that another physical mechanism is at play in the generation of this structure. In this respect, it is encouraging to compare the observed streamwise wavelength of the cross-streamwise velocity structure with that of the streak instability in the previous theoretical analysis. The stability analysis using an eddy-viscosity model (Park *et al.* 2011) predicted that a streaky base flow with $\lambda_z/h = 4$ becomes unstable at $\lambda_x/h \simeq 3-6$. At first glance, this prediction does not seem to match well with $\lambda_x/h \simeq 1-2$ in the present numerical experiment. However,

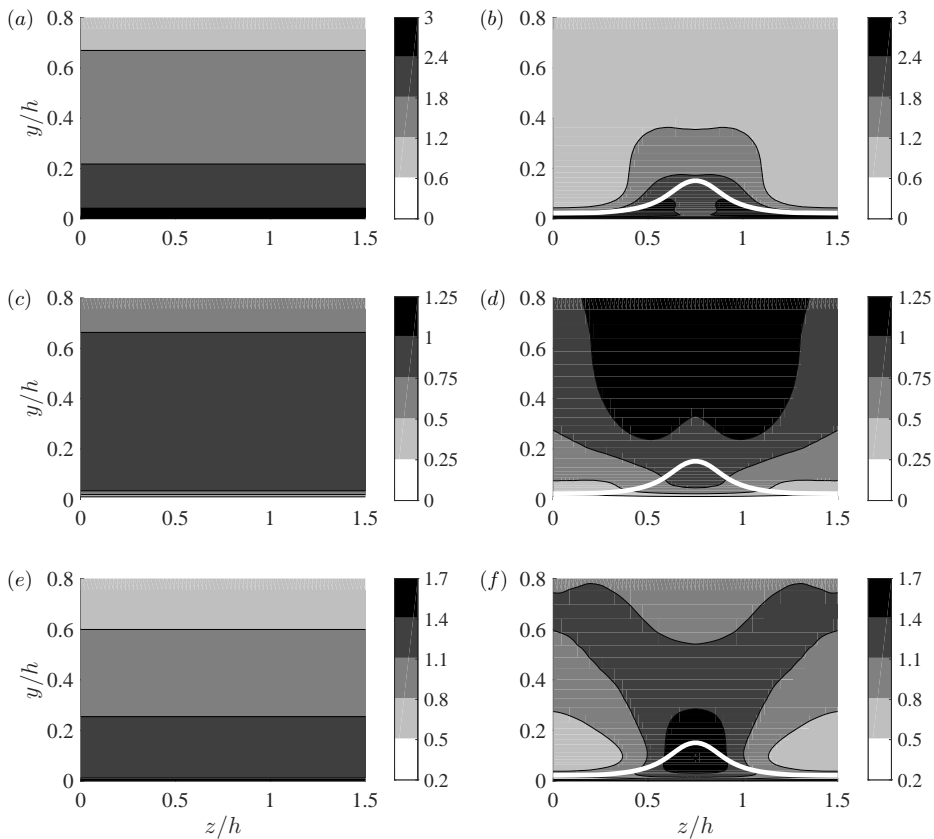


FIGURE 8. Cross-streamwise view of the rms of the velocities for (a, c, e) $A_s^+ = 0$ and (b, d, f) $A_s^+ = 3.42$ (S960): (a, b) streamwise velocity; (c, d) wall-normal velocity; (e, f) spanwise velocity. The thick white line indicates the location where the cross-streamwise mean velocity is $0.9U_c$ (U_c is the centreline velocity of the simulation).

the spanwise spacing of the streak in the present study is $\lambda_x/h \simeq 1.5$, considerably smaller than $\lambda_z/h = 4$ in Park *et al.* (2011). Indeed, a recent extension of the theoretical analysis to smaller spanwise wavelengths showed that there exists a self-similar relation between the spanwise wavelength of the imposed streak and the streamwise wavelength of its instability (Alizard 2015). If this is adopted, a streak at $\lambda_z/h \simeq 1.5$ would become unstable at $\lambda_x/h \simeq 1.13 - 2.25$, showing a fairly good agreement with $\lambda_x/h \simeq 1 - 2$ observed in the present study.

Further evidence of the streak instability mechanism is found in the cross-streamwise view of the velocity fluctuations in figure 8, where the left and right columns visualise the unforced and forced cases, respectively. We remind the reader that the streaky mean flow shows an even symmetry about $z/h = 0.75$ (figure 4) and that the eigenstructure of a sinuous-mode streak instability is mathematically defined by odd symmetry of the streamwise and wall-normal velocities and by even symmetry of the spanwise velocity

about this axis (see e.g. Andersson *et al.* 2001): i.e.

$$\begin{aligned}\check{u}(y, z^*) &= -\check{u}(y, -z^*), \\ \check{v}(y, z^*) &= -\check{v}(y, -z^*), \\ \check{w}(y, z^*) &= \check{w}(y, -z^*),\end{aligned}\tag{3.5}$$

with $z^* = z - 0.75h$. Here, $\check{\mathbf{u}}(y, z^*) = (\check{u}, \check{v}, \check{w})$ is the eigenfunction of the streak instability, and the instability mode in physical space is constructed as $\hat{\mathbf{u}}(y, z^*)e^{ik_{x,m}x}$ ($k_{x,m}$ is the streamwise wavenumber of the instability). Given the mathematical definition, the streamwise and wall-normal velocity fluctuations solely from the sinuous-mode instability should be zero along $z/h = 0.75$ and the spanwise velocity fluctuation is supposed to have a local maximum/minimum along this axis. Therefore, in the presence of background turbulence, the streamwise and wall-normal velocity fluctuations of the sinuous-mode instability would always show a local minimum along $z/h = 0.75$, while the spanwise one should exhibit a local maximum/minimum along this axis. These features indeed appear in the computed cross-streamwise view of turbulent velocity fluctuations in figure 8: both the streamwise and wall-normal velocity fluctuations exhibit two symmetric peaks with a local minimum given along $z = 0.75h$ (figures 8*b,d*), while the spanwise one shows a local maximum along $z/h = 0.75$ (figure 8*f*). We also note that the cross-streamwise view of the velocity fluctuations is qualitatively the same as the one in a laminar boundary layer (Andersson *et al.* 2001), indicating the presence of a sinuous-mode instability. In §3.3, we will provide further evidence of the sinuous-mode instability by visualising the most energetic DMD mode (see figure 11).

3.3. Dynamic mode decomposition

A DMD is performed to examine the flow structure in detail. For the snapshots of the DMD, a time series of a specific Fourier component of the velocity field in the lower half of the wall-normal domain is taken from the simulation with a sufficiently large streak amplitude. The spanwise wavenumber is chosen to be the same as that of the forcing ($k_z = 2\pi/\lambda_z$ with $\lambda_z/h = 1.5$), while a range of different streamwise wavenumbers ($k_x = 2\pi/\lambda_x$) are considered ($2 < \lambda_x/h < 5$). For given k_z and k_x , each snapshot is constructed such that:

$$\bar{\mathbf{u}}(y, z; k_x) = \hat{\mathbf{u}}(y; k_x, k_z)e^{ik_z z} + \hat{\mathbf{u}}(y; k_x, -k_z)e^{-ik_z z}.\tag{3.6}$$

We note that $\bar{\mathbf{u}}(y, z; k_x)$ is the streamwise Fourier component given only with $\pm k_z$ spanwise Fourier components. The DMD modes and the corresponding eigenvalues μ_j are then computed following the procedure in §2.2. The time interval, the number of POD modes and the number of snapshots for the DMD are carefully chosen to ensure good temporal resolution of large-scale dynamics: $\Delta t u_\tau/h = 0.009$, $r = 30$ and $N = 1000$ (see Appendix A for a detailed discussion on the choice of parameters). Once the DMD is performed, the associated angular frequency is computed by taking the real part of $\omega_j = i \ln \mu_j / \Delta t$. Since the snapshot in (3.6) represents a streamwise Fourier component, the downstream propagating speed of the DMD mode is computed by

$$c_j = \frac{\omega_j}{k_x},\tag{3.7}$$

where c_j is the phase speed of the j -th DMD mode. The relative amplitude α_j of all of the DMD modes is finally determined (see also §2.2).

The DMD result of the S960 simulation is shown in figure 9 for $\lambda_x/h = 3.57$ and $A_s^+ = 3.42$. The DMD modes are deemed to be neutral, given that the eigenvalues μ_j

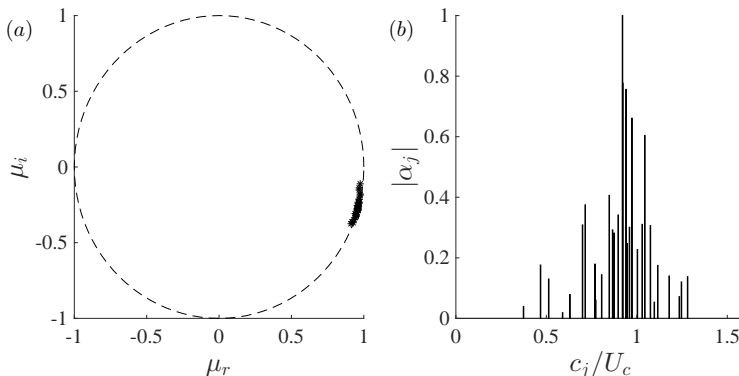


FIGURE 9. DMD analysis with $\lambda_x = 3.57h$ for $A_s^+ = 3.42$ (S960): (a) eigenspectra in the μ_r - μ_i plane; (b) mode amplitude $|\alpha_j|$ with phase speed c_j (the mode amplitude is normalised by the largest one).

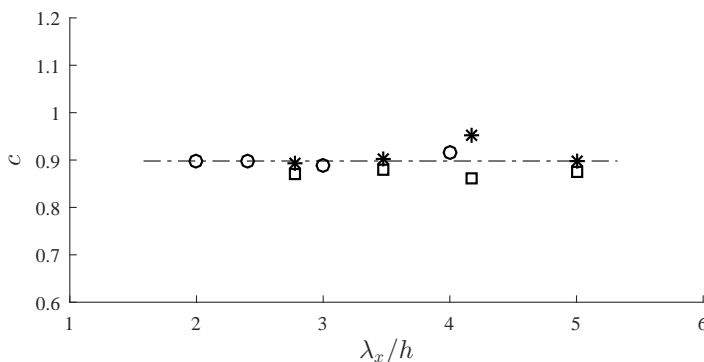


FIGURE 10. Variation of phase speed (c/U_c) with streamwise wavelength: \square , $A_s^+ = 4.11$ (S490), $*$, $A_s^+ = 4.04$ (S960); \circ , $A_s^+ = 3.77$ (S2050). Here, the horizontal line indicates $c = 0.9U_c$.

sit well on the unit circle (figure 9a). This also indicates that the snapshots are indeed collected from a statistically stationary flow with a good resolution. Their asymmetry is due to the processing of complex-valued snapshots instead of real-valued ones. Using (3.7), the computed eigenvalues are subsequently transformed to the phase speed of the DMD modes. The contribution of each DMD mode is then assessed by computing its amplitude α_j , as shown in figure 9(b). The phase speed of the DMD modes appears mainly in the range of $0.7 \lesssim c/U_c \lesssim 1.1$ (U_c is the centreline velocity of each simulation), and, in particular, the most energetic DMD mode exhibits $c/U_c \simeq 0.9$.

It is important to mention that the computed phase speed of the most energetic DMD mode is found to not significantly depend on the streamwise wavelength and the Reynolds number, as long as the streak amplitude is chosen to be $A_s^+ > 3$. Fig. 10 shows the phase speed of the most energetic DMD mode with respect to the streamwise wavelength for all the considered Reynolds numbers. It appears that the most energetic DMD mode, for different streamwise lengths and Reynolds numbers, robustly exhibits $c/U_c \simeq 0.9$. This suggests that the propagation speed of the flow structure generated by the streak instability scales well with the centreline velocity, consistent with del Álamo & Jiménez (2009) who showed the outer scaling of the propagation speed of large-scale structures.

Finally, the most energetic DMD mode is examined. Fig. 11 (a) and (b) show the

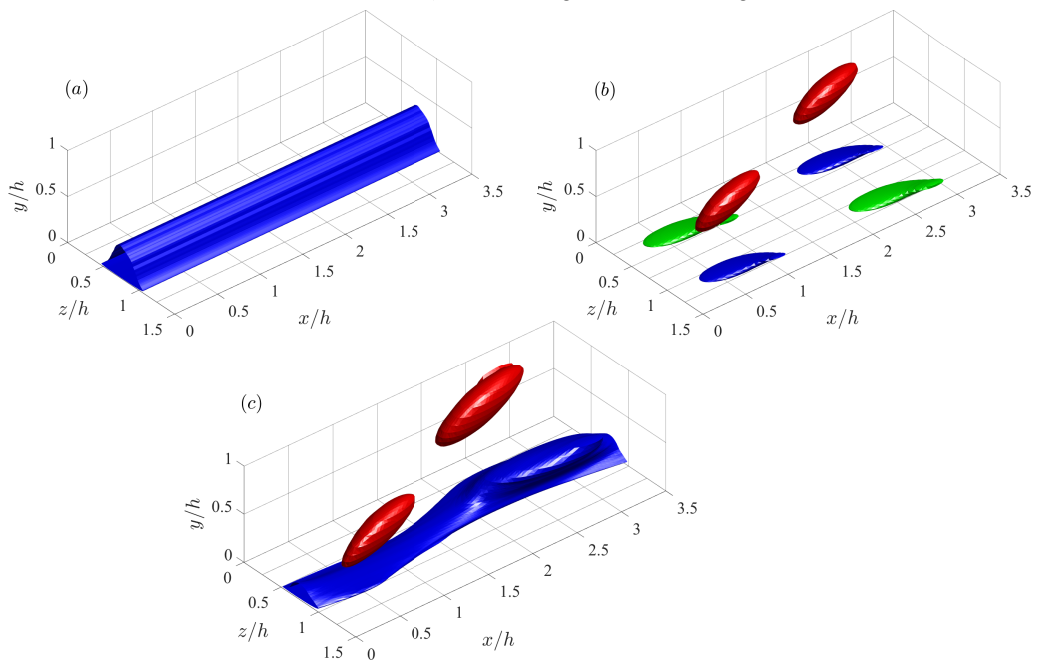


FIGURE 11. Visualisation of the streak instability using the most energetic DMD mode from the S960 simulation ($\lambda_x/h = 3.73$ and $A_s^+ = 4.73$): (a) the low-speed streak with $u'_s = -0.03U_c$ ($u'_s \equiv u_s(y, z) - \langle u_s(y, z) \rangle_z$ where $\langle \cdot \rangle_z$ denotes average in the spanwise direction); (b) the DMD mode \mathbf{u}_{dmd} where the green iso-surfaces are a positive streamwise velocity ($0.8 \max[u_{dmd}]$), the blue ones a negative streamwise velocity ($u = 0.8 \min[u_{dmd}]$), and the red ones a negative wall-normal velocity ($v = 0.8 \min[v_{dmd}]$); (c) the low-speed streak with the DMD mode ($\mathbf{u}_s - \langle \mathbf{u}_s \rangle_z + \gamma \mathbf{u}_{dmd}$ where γ is an appropriate tuning constant for visualisation). In (c), the blue iso-surface indicates a negative streamwise velocity, while the red ones indicate a negative wall-normal velocity.

streaky uniform mean flow and the most energetic DMD mode for $\lambda_x/h = 3.73$, respectively, and their combination is given in figure 11 (c). Fig. 11 (c) clearly reveals that the structure is composed of a streamwise meandering low-speed streak (blue isosurface in figure 11c) and a streamwise-alternating pattern of wall-normal velocity structures (red iso-surface in figure 11c). We note that this is a robust feature of the computed DMD mode and it does not significantly depend upon the choice of the DMD parameters, such as the streamwise wavelength λ_x , the number of snapshots N , and the number of POD modes r . Therefore, the spatial structure of the DMD mode in figure 11 clearly indicates that the flow structure with an intense cross-streamwise turbulent kinetic energy in §3.2 is directly linked to the sinuous-mode streak instability. In this respect, it is finally worth mentioning that the structure of the most energetic DMD mode with the streaky mean flow highly resembles the general form of the traveling-wave solutions in Hwang *et al.* (2016), which is a mathematical representation of the self-sustaining process.

4. Discussion

Thus far, we have explored the instability mechanism of an ‘amplified’ streak in the outer region (VLSM) and its mode as the initiating physical process of LSMs. A body forcing, designed to drive an infinitely long streak (Hwang & Cossu 2010a), is implemented in a set of numerical simulations. As the forcing amplitude is increased,

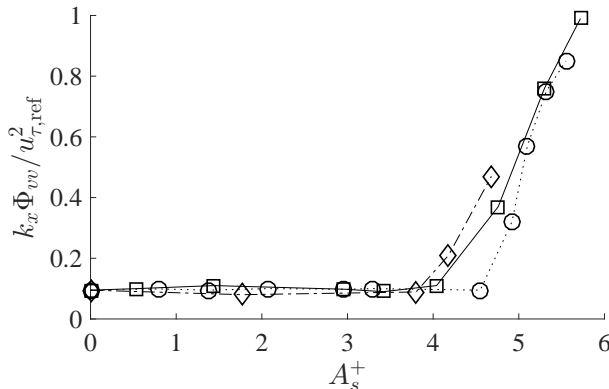


FIGURE 12. Premultiplied streamwise wavenumber spectral intensity of wall-normal velocity with the streak amplitude at $y/h = 0.64$ for $\lambda_x/h = 3.57$: \circ , S490; \square , S960; \diamond , S2050.

a long streaky structure, which resembles a VLSM, emerges. It is shown that the presence of such a long streaky structure in the outer region generates an intense cross-streamwise velocity structure at $\lambda_x/h \simeq 1 - 2$, and this streamwise length scale shows good agreement with that predicted by the previous stability analysis (Park *et al.* 2011; Alizard 2015). The cross-streamwise view of the turbulence statistics has also revealed that this structure has features mathematically consistent with the sinuous-mode streak instability. Finally, a DMD analysis shows that this structure is characterised by a streamwise meandering motion of the driven streak and alternating cross-streamwise velocity structures, indicating that the cross-streamwise velocity structure at $\lambda_x/h \simeq 1 - 2$ is a consequence of the sinuous-mode streak instability.

The present numerical experiment is specifically designed to observe the streak instability, while taking the nonlinearity of the governing equation and background turbulence fully into account. This is achieved by artificially driving a streak with the optimal forcing, but we note that this does not allow the driven streak to break down. For this reason, in the present numerical experiment, the nonlinearly evolved streak instability and the accompanying vortical structures coexist. Therefore, with the present numerical experiment alone, it is difficult to precisely explain the causal relation between the streak instability and the vortical structures. However, as we shall see in §4.3, the sinuous-mode streak instability essentially originates from the spanwise shear created by the presence of the driven large-amplitude streak. This implies that the streak instability is the seeding mechanism of the vortical structures, and this interpretation is consistent with Hwang & Bengana (2016), where the emergence of the streak instability prior to the vortical structures is clearly identified with the minimal-unit simulation.

In many ways, the flow structure emerging at $\lambda_x/h \simeq 1 - 2$ via the streak instability is remarkably similar to the LSM. Firstly, its streamwise length scale and wall-normal location (figures 6 and 7) are in good agreement with those of the LSM (Kovaszny 1970; Monty *et al.* 2009). Secondly, the structure is mainly featured by intense wall-normal and spanwise turbulent kinetic energy, as the LSM is in a real flow (Hwang 2015). Thirdly, a series of the cross-streamwise velocity components of this structure are collectively aligned along the low-speed streak (figure 11c), consistent with the early view of a VLSM as a concatenation of adjacent LSMs (e.g. Kim & Adrian 1999; Baltzer *et al.* 2013). However, it should be mentioned that the present numerical experiment provides a different interpretation of the relation between the LSM and the VLSM: the reason

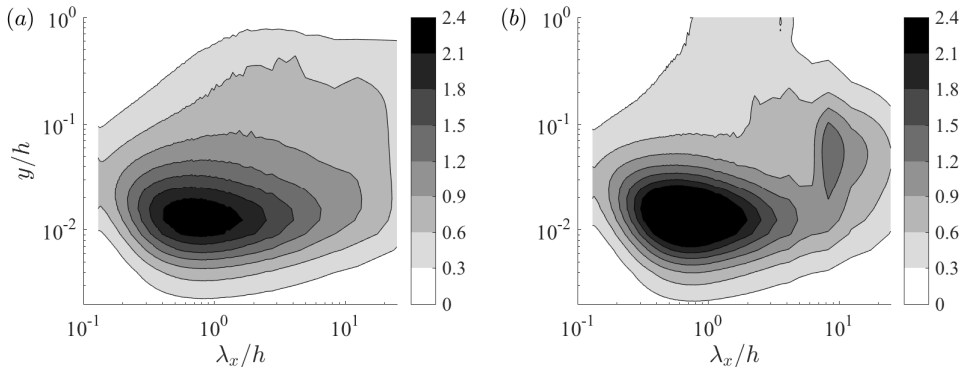


FIGURE 13. Premultiplied streamwise wavenumber spectra of streamwise velocity (S960); (a) unforced case; (b) $A_s^+ = 4.04$.

that a VLSM appears as a concatenation of a number of LSMs is because a series of the LSMs are formed along a long VLSM by the streak instability. Lastly, the emergence of the sinuous-mode instability implies that the VLSM would meander along the streamwise direction (figures 2 and 11), as previously observed in Hutchins & Marusic (2007).

All of these observations suggest that the LSM is initiated by the sinuous-mode instability of the amplified streak in the outer region (VLSM). This interpretation is well integrated into the self-sustaining nature of the large-scale structures composed of VLSMs and LSMs (Hwang & Cossu 2010c; Hwang 2015; Hwang & Bengana 2016; Hwang *et al.* 2016), and is also consistent with the previous theoretical studies on the streak instability (Park *et al.* 2011; Alizard 2015). There have been several different propositions on the formation mechanism of the LSM, such as the mergers/growth mechanism (Perry *et al.* 1986; Zhou *et al.* 1999; Adrian 2007) and the Orr mechanism (Jiménez 2013*a,b*). However, it should be stressed that, to the best of our knowledge, only the streak instability mechanism currently explains the streamwise length-scale determination of the LSM among these different propositions.

4.1. Emergence of streak instability at large scales

In the near-wall region, it has been shown that the streak instability is subcritical, admitting strong transient growth at low streak amplitudes before the onset of a normal-mode instability (Schoppa & Hussain 2002). Consistent with this, our recent work has shown that the streak instability and the related near-wall quasi-streamwise vortices at $\lambda_x^+ \simeq 200-300$ spontaneously emerge on increasing the streak amplitude (Cassinelli *et al.* 2017), exhibiting a sensitive response to the initial condition and/or external noise, as is typically observed in a highly non-normal system (Schmid & Henningson 2001). However, it should also be mentioned that such non-normal growth of the perturbation around a low-amplitude streak is typically an outcome of the interaction with the marginally stable sinuous mode. Therefore, in practice, distinguishing the transient growth from the normal-mode instability is almost impossible at least for near-wall turbulence and for transitional laminar boundary layers, as pointed out by Hoepffner *et al.* (2005).

To carefully examine the emergence of the streak instability in the present numerical experiment, the one-dimensional spectral intensity of the wall-normal velocity for $\lambda_x/h = 3.57$ is plotted in figure 12 against the streak amplitude. For relatively low streak amplitudes ($A_s^+ < 4$), the intensity of the wall-normal velocity is very slightly elevated. However, when the streak amplitude reaches $A_s^+ \simeq 4$, the spectral intensity drastically

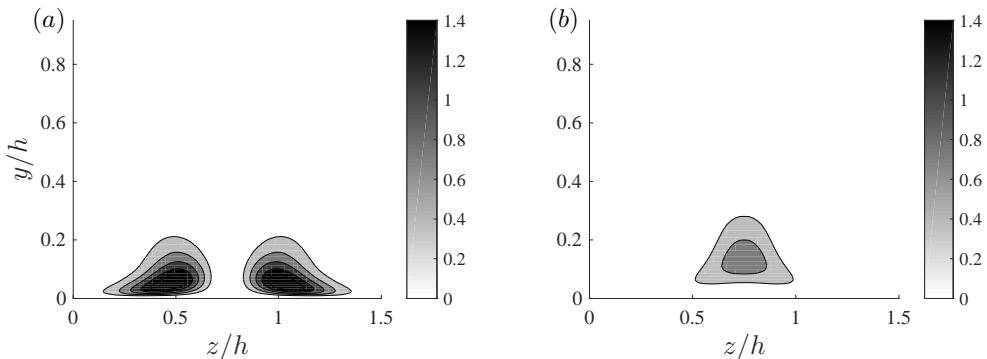


FIGURE 14. Turbulent kinetic-energy production around the streaky mean flow for $A_s^+ = 3.42$ (S960): (a) $-\langle u'w' \rangle_{x,t} \partial \bar{U}^+(y,z)/\partial z$; (b) $-\langle u'v' \rangle_{x,t} \partial \bar{U}^+(y,z)/\partial y$.

increases for all the Reynolds numbers considered. This behaviour is very interesting, as it indicates that the onset of a normal-mode instability would be $A_s^+ \simeq 4$. However, this does not imply that the streaky motion in a real flow (VLSM) would experience such a normal-mode instability for $A_s^+ \gtrsim 4$. Firstly, as is evident in figure 12, the typical spectral intensity of the wall-normal velocity in the unforced simulation is much smaller than that observed for $A_s^+ \gtrsim 4$. Secondly, the spectra of the wall-normal velocity in the unforced simulation do not exhibit high intensity for $\lambda_x > 5 - 10h$ in the outer region (figure 6a). However, the forced simulations with $A_s^+ \gtrsim 4$ show much higher spectral intensity in this range of the streamwise wavelength (figures 6f-h). Finally, the forced simulations with relatively low streak amplitudes ($A_s^+ \lesssim 4$) are not actually unresponsive to the surrounding perturbations: the wall-normal velocity spectra of the simulations with $3 \lesssim A_s^+ \lesssim 4$ also exhibit a fairly energetic peak at $\lambda_x/h \simeq 1 - 2$ (figures 6d-f), which would be more consistent with the spectra of the unforced reference simulation.

These observations suggest that VLSMs in a real flow are unlikely to reach $A_s^+ \gg 4$ because they should break down quickly with the emergence of the streak instability (Hwang & Bengana 2016). The streak amplitude would reach at best $A_s^+ \simeq 4$, below which the wall-normal velocity structure is excited primarily at $\lambda_x/h \simeq 1 - 2$. This also indicates that the streak instability process in the outer region may be mainly driven by a non-modal mechanism (secondary transient growth), as that in the near-wall region. Finally, it should be stressed that the wall-normal velocity structure at $\lambda_x/h \simeq 1 - 2$ is the first feature noticeable statistically on increasing the streak amplitude, and it depends very little on the type of body forcing that drives the streak. This issue will be further discussed in §4.4.

4.2. The streamwise length scale of very large-scale motion

The present numerical experiment also provides important physical insight into the streamwise length scale determination of the VLSM. If the streak amplitude is given by $3 \lesssim A_s^+ \lesssim 4$ just before the breakdown phase in the self-sustaining process (see also the discussion in §4.1), the largest streamwise wavelength of the wall-normal velocity structure generated by the streak instability mechanism would be limited to $\lambda_x/h \simeq 10 - 20$ (see figures 6d-f). The generated wall-normal velocity structure would then trigger linear amplification of the streaky structures that mainly carry the streamwise turbulent kinetic energy (i.e. lift-up effect). As discussed in §2.1, the largest possible linear amplification of the streaks takes place at infinitely long streamwise wavelength

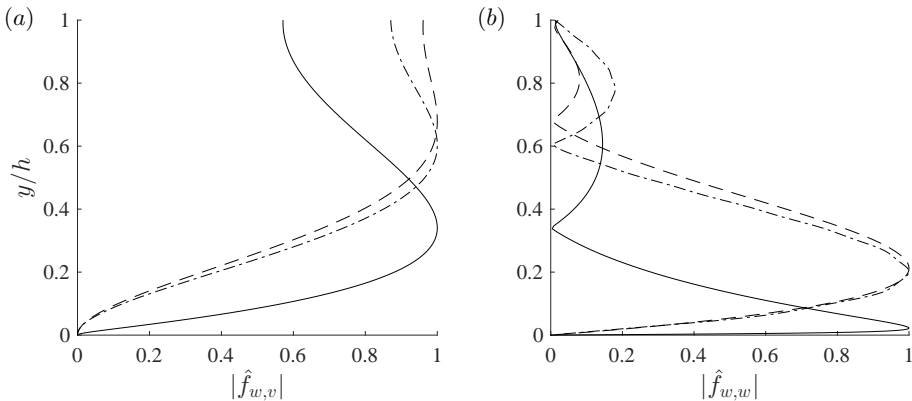


FIGURE 15. The wall-normal profile of the optimal forcing with three different eddy viscosities in (2.2): (a) $|\hat{f}_{w,v}|$, (b) $|\hat{f}_{w,w}|$. Here, —, the Cess eddy viscosity ($\nu_t = \nu_t(y)$ in (2.3)); - · - · -, a constant eddy viscosity ($\nu_t = \max_y \nu_t(y)$); - - -, no eddy viscosity ($\nu_t = 0$).

and it generally prefers longer streamwise length for larger amplification (del Álamo & Jiménez 2006; Pujals *et al.* 2009; Cossu *et al.* 2009; Hwang & Cossu 2010*b*; Willis *et al.* 2010). Therefore, the largest admissible streamwise wavelength of the streak instability (i.e. $\lambda_x/h \simeq 10 - 20$) is expected to determine the streamwise length scale of the VLSM.

This scenario is examined in figure 13, where the streamwise wavenumber spectra of the streamwise velocity for both the unforced and forced simulations are shown. Here, the streak amplitude of the forced simulation is chosen to be $A_s^+ = 4.04$, as the excitation of the wall-normal velocity structure around $\lambda_x/h \simeq 10$ is well visible at this amplitude (see figure 6*f*). As expected from the wall-normal and spanwise velocity spectra (figures 6 and 7), the streamwise velocity spectra of the forced simulation reveal elevated spectral intensity at $\lambda_x/h \simeq 1 - 2$ and $y/h \gtrsim 0.3$ (figure 13*b*), the location associated with the LSM (figure 13*a*). However, in the streamwise velocity spectra of the forced simulation (figure 13*b*), there exists another more distinct peak at $\lambda_x/h \simeq 10$ throughout the logarithmic layer. Importantly, the wall-normal location and the streamwise wavelength of this peak are very close to those of the VLSM, directly supporting the notion that the largest streamwise wavelength of the streak instability determines the streamwise length scale of the VLSM.

4.3. Physical mechanism of streak instability

The second-order cross-streamwise statistics and the DMD analysis suggest that the vortical structure at $\lambda_x/h \simeq 1 - 2$ originates from the sinuous-mode streak instability in the form of a streamwise meandering streak and alternating cross-streamwise velocity components (figure 11*c*). The sinuous-mode instability is understood to be an energy-production process from the spanwise mean shear via the inflectional mechanism (e.g. Park & Huerre 1995). To investigate this feature of the sinuous-mode instability in the present numerical experiment, turbulent production by the streaky mean flow are further examined in this section. The streaky mean flow is defined as $\bar{U}(y, z) = U_0(y) + \tilde{u}(y, z)$ because the mean flow is dominated by the streamwise component (see the discussion in §3.1). Turbulent production around such a mean flow are given by $-\langle u'w' \rangle_{x,t} \partial \bar{U}^+ / \partial z$ and $-\langle u'v' \rangle_{x,t} \partial \bar{U}^+ / \partial y$; the former indicates production by the spanwise mean shear, while the latter is production by the wall-normal mean shear. The two turbulent kinetic-energy production mechanisms are visualised in figure 14. Production by the spanwise

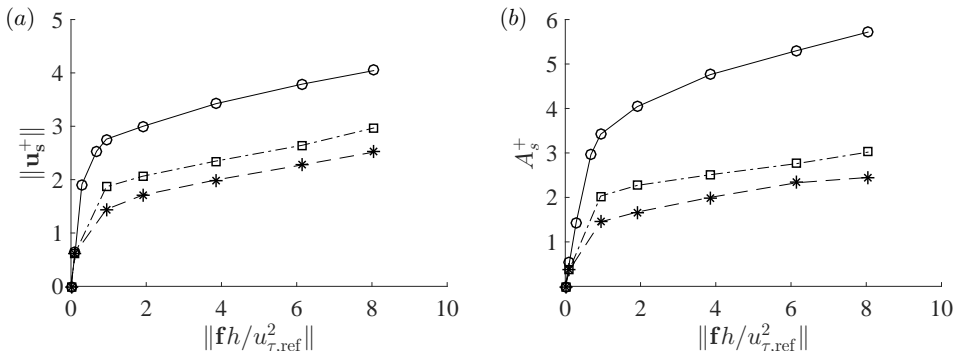


FIGURE 16. Flow response to the forcing for S960: (a) $\|\mathbf{u}_s^+\|$; (b) A_s^+ . Here, \circ , the Cess eddy viscosity ($\nu_t = \nu_t(y)$ in (2.3)); $*$, no eddy viscosity ($\nu_t = 0$); \square , a constant eddy viscosity ($\nu_t = \max_y \nu_t(y)$).

shear appears at either side of the low-speed region at $z/h = 0.75$ (figure 14a), whereas that by the wall-normal shear is strong only in the top of the low-speed region (figure 14b). In this figure, it is evident that production by the spanwise shear is much greater than that by wall-normal shear, confirming that the streak instability in the present study is a sinuous mode.

4.4. Robustness to the forcing profile

Thus far, the optimal forcing employed in the present study is obtained using the linearised Navier-Stokes equation with the eddy viscosity in (2.3). However, it should be pointed out that this forcing is not the only type of the forcing that can generate a streak. Indeed, the only requirement for body forcing to generate a streak is to contain reasonably strong cross-streamwise components, given the mechanism of the streak formation (i.e. the lift-up effect). In this section, we therefore consider two additional forcing profiles to examine the robustness of the present result: one is the optimal forcing computed without eddy viscosity ($\nu_t = 0$), and the other is obtained by setting $\nu_t = \max_y(\nu_t(y))$. We note that these different eddy viscosities are introduced only for the linear theory in order to generate different types of forcing. Unsurprisingly, the optimal forcing with the two different eddy viscosities are also found to consist of a pair of counter-rotating streamwise vortices (not shown; see also the discussion in §2.1). However, as shown in figure 15, their wall-normal profiles significantly differ from that of the original optimal forcing. While the wall-normal profiles of the two new forcings are not very different from each other, they have much larger values in the location much further from the wall: indeed, the wall-normal component of the two forcings show a maximum at $y/h \simeq 0.6$, whereas the optimal forcing with the original Cess viscosity exhibits its peak at a location much closer to the wall, $y/h \simeq 0.35$.

The response to the three different types of the forcing was then examined, as reported in figure 16. While all the three forcings are found to robustly generate the streaky motion (not shown; see also the discussion in §2.1), the optimal forcing obtained with the Cess eddy viscosity gives rise to a significantly larger response of the streamwise velocity component. This implies that the linearised Navier-Stokes equation with the Cess eddy viscosity provides a much better description of the linear process in a real turbulent flow than the other two cases with different eddy viscosities. This also suggests that the streaky motion generated by the optimal forcing with the Cess eddy viscosity would be

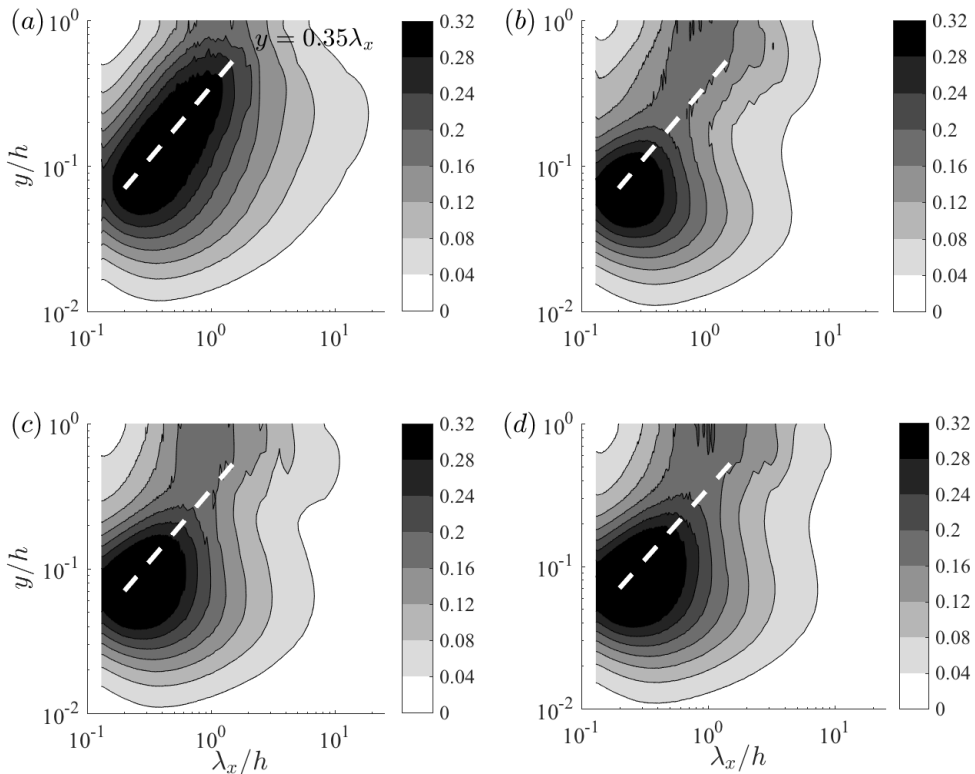


FIGURE 17. Premultiplied streamwise wavenumber spectra of wall-normal velocity (S960). (a) $A_s^+ = 0$ (unforced); (b) $A_s^+ = 3.42$ with the Cess eddy viscosity ($\nu_t = \nu_t(y)$ in (2.3)); (c) $A_s^+ = 1.47$ with no eddy viscosity ($\nu_t = 0$); (d) $A_s^+ = 2.04$ with a constant eddy viscosity ($\nu_t = \max_y \nu_t(y)$). Here, the thick white dashed line indicates $y = 0.35\lambda_x$.

the closest to the one in a real flow, because it implies that such a streaky motion can be most easily generated by the nonlinear term.

Here, it should be stressed that this interesting behaviour originates from an important physical feature of the Cess eddy viscosity, which satisfies the following mixing length hypothesis:

$$\nu_t \frac{dU}{dy} = -\overline{u'v'}. \quad (4.1)$$

In the logarithmic region, $dU/dy \sim 1/y$ and the Reynolds shear stress is approximately constant. Therefore, the considered $\nu_t(y)$ should grow linearly with y in the logarithmic region according to (4.1). It should be pointed out that this tendency of ν_t must be generic in any turbulence model for wall-bounded shear flows. In the near-wall region, both the integral and dissipation length scales are the inner length scale ν/u_τ , indicating that the dissipation process should be dominated by the molecular viscosity. On the other hand, in the outer region, the integral length scale (h) is largely separated from the dissipation length scale $((\nu^3 h/u_\tau^3)^{1/4})$, and this length-scale separation is given by the ratio of the integral scale to the dissipation scale, i.e. $Re_\tau^{3/4}$. Therefore, in the outer region, the energy dissipation takes place through the Richardson-Kolmogorov cascade,

requiring large ν_t from the modelling viewpoint. In the logarithmic region, the only way to smoothly connect the two very different dissipation mechanisms in the near-wall and outer regions is by having monotonically increasing ν_t in the wall-normal direction, as reflected in (4.1). This behaviour of ν_t explains why the optimal forcing obtained with the Cess eddy viscosity has large values in the region close to the wall – the large value of the forcing should generate a large response due to the small eddy viscosity in this region. It has been recently shown that this behaviour of ν_t is essential for understanding the scaling of coherent structures in the logarithmic and outer regions (Hwang 2016): for example, the Reynolds-number-dependent scaling of the peak wall-normal location of streamwise turbulence intensity, the near-wall penetration of the large-scale outer structures, and the incomplete self-similarity of the streamwise and spanwise velocity components of the coherent structures in the logarithmic region.

By applying the three different types of optimal forcing in figure 16 to a numerical simulation, the sensitivity of the streak instability was finally examined. Fig. 17 shows the streamwise wavenumber spectra of the wall-normal velocity when each of the three optimal forcings just begins to exhibit streak instability. Here, the forcing amplitude follows the definition of (3.1), and the corresponding responses are evaluated using (3.3) and (3.4). Despite the difference in the forcing profiles shown in figure 15, the streamwise wavenumber spectra of the wall-normal velocity reveal that the energetic vortical structures at $\lambda_x \simeq 1 - 2h$ in the outer region emerge in all the three cases (figures 17*b,c,d*). This clearly indicates that the streak instability is a very robust physical process that depends very little on the type of the forcing, as long as the forcing is kept to generate an amplified streak in the outer region.

5. Concluding remarks

Thus far, we have examined the instability of an ‘amplified’ streaky motion artificially driven by the optimal forcing computed in Hwang & Cossu (2010*a*). As the forcing amplitude is gradually increased, a streamwise-uniform streak, reminiscent of VLSM, is successfully introduced. We have shown that an energetic cross-streamwise velocity structure emerges at the streamwise length scale $\lambda_x/h = 1-2$, and this structure produces all statistical features of the LSM remarkably. All diagnosis tools employed (the cross-streamwise turbulence statistics, DMD analysis and energy-production analysis) firmly indicate that the origin of this structure is a sinuous-mode streak instability. Finally, it has been proposed that the streak instability mechanism determines the streamwise length scales of the LSM and the VLSM.

It is evident that the present numerical experiment directly supports the existence of the self-sustaining process in the outer region (Hwang & Cossu 2010*c*; Hwang 2015; Hwang & Bengana 2016). In particular, it should be noted that the DMD structure given in figure 11 (c) is remarkably similar to the invariant solution in Hwang *et al.* (2016). However, the most important contribution of the present study is that it provides direct evidence of the streak instability process, the existence of which has only been speculated for many years. The present study also unveils the importance of nonlinear processes in understanding the mechanism of the streamwise length-scale determination, and this may play a crucial role in developing low-order models for coherent structures at high Reynolds numbers. Finally, it should be mentioned that the present approach can be extended to the logarithmic region, where the self-sustaining process has been recently shown to emerge in a hierarchical manner (Hwang 2015; Hwang & Bengana 2016). Our efforts are focused in this direction, and we believe that this will unveil the in detail

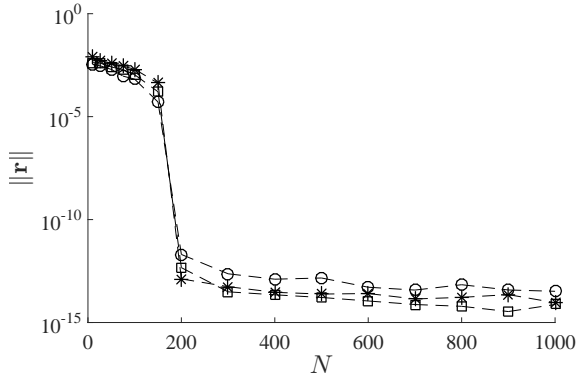


FIGURE 18. The norm of the residual vector with the number of snapshots N (S960): *, $A_s^+ = 3.42$; \square , $A_s^+ = 4.04$; \diamond , $A_s^+ = 4.76$.

formation mechanism of the self-similar vortex clusters in the logarithmic region (del Álamo *et al.* 2006).

Acknowledgements

This work was supported by the Engineering and Physical Sciences Research Council (EPSRC) in the UK (EP/N019342/1). We also thank the anonymous reviewers for a number of useful suggestions.

Appendix A. Dynamic Mode Decomposition

As stated in §2.2, the parameters for the DMD need to be chosen very carefully. Hereafter, we discuss how we have chosen the three main parameters of the DMD: i.e. the sampling time-interval Δt , the number of snapshots N , and the number of POD modes r .

A.1. Sampling time interval Δt

The theoretical upper bound for the sampling time step is represented by the Nyquist criterion, which applies to the frequency of the process we are interested in (i.e. streak instability). There is also a lower bound, since a too high sampling rate could result in this feature being perceived as quasi-steady (Schmid 2010). The typical time scale of the self-sustaining process in the outer layer is $T_{ssp}u_\tau/h \simeq 3$ and the time scale of the streak instability is even shorter (Hwang & Bengana 2016). To provide a good resolution for this time scale, four different snapshot time intervals have been tested with S960: $\Delta tu_\tau/h = 0.009, 0.018, 0.027, 0.036$. The two smaller values yield eigenvalues of \mathbf{S} lying almost perfectly on the unit circle $|\mu| = 1$ (see figure 9), and the smallest value has been used for the DMD analysis in the present study.

A.2. Total number of snapshots N

The minimum number of snapshots N is determined as follows. We first assume that the N -th snapshot is given by a linear combination of all previous $N - 1$ snapshots with a residual vector \mathbf{r} : i.e.

$$\psi_N = \Psi_0 \mathbf{a} + \mathbf{r}, \quad (\text{A } 1)$$

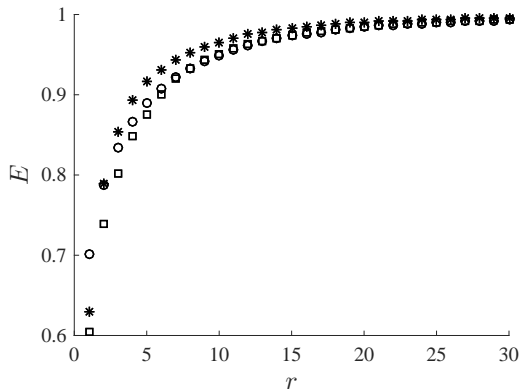


FIGURE 19. Energy content of the first r POD modes (S960): *, $A_s^+ = 3.42$; □, $A_s^+ = 4.04$; ◇, $A_s^+ = 4.76$.

where $\mathbf{a} = [a_1 \ a_2 \ \dots a_{N-1}]^T$ is a column vector for the coefficients of the linear combination. If the norm of \mathbf{r} approaches zero for sufficiently large N , the number of snapshots may be considered large enough to cover any flow field using the snapshots. The minimum residual \mathbf{r} is computed with the economy-size QR decomposition of the snapshots $\Psi_0 = \mathbf{Q}\mathbf{R}$, and the coefficients of the linear combination are given by

$$\mathbf{a} = \mathbf{R}^{-1}\mathbf{Q}^H\psi_N. \quad (\text{A } 2)$$

The residual and its 2-norm are then found with (A 1) and (A 2).

Fig. 18 shows the dependence of the 2-norm of \mathbf{r} on the number of snapshots. The test was carried out with $\Delta t u_\tau/h = 0.009$ using the S960 simulations with three different forcing amplitudes. At $N \simeq 200$, the 2-norm of the residual vector drops drastically, and falls below $O(10^{-10})$. However, further increase in the number of snapshots N does not decrease the residual vector significantly, and it remains at $O(10^{-15})$ even for $N = 1000$. The number of snapshots chosen in the present study is $N = 1000$. We note that this number also ensures that the total time interval of the snapshots is $Tu_\tau/h \simeq 9$, which would be six to nine times longer than the streak meandering time scale observed in Hwang & Bengana (2016).

A.3. Number of POD modes r

The choice of the number of POD modes to be included has been based on the amount of energy contained in the first r POD modes. Here, $N = 1000$ and $\Delta t u_\tau/h = 0.009$, and the calculations were performed with the S960 simulations. If the matrix of snapshots is decomposed as $\Psi_0 = \mathbf{U}\Sigma\mathbf{V}^H$, the relative energy content up to the r^{th} mode is computed by:

$$E = \frac{\sum_{i=1}^r \Sigma_{ii}}{\text{trace}(\Sigma)}. \quad (\text{A } 3)$$

Fig. 19 reports the dependence of E on r . With only the first twenty-five modes, more than 95% of the total energy is recovered. Given this feature, it is evident that the use of all the POD modes is not necessary. Furthermore, appropriate truncation of the number of POD modes would help for eliminating noise associated with background turbulence, as higher-order POD modes are expected to contain such noise. Therefore, in the present study, thirty POD modes are used to ensure to contain all the energetic features in our

DMD analysis, while appropriately removing the effect of noisy small-scale background in the snapshots.

REFERENCES

- ADRIAN, R. J. 2007 Hairpin vortex organization in wall turbulence. *Phys. Fluids* **19** (4), 041301.
- ADRIAN, R. J., BALACHANDAR, S. & LIU, Z. C. 2001 Spanwise growth of vortex structure in wall turbulence. *KSME Int. J.* **15** (12), 1741–1749.
- DEL ÁLAMO, J. C. & JIMÉNEZ, J. 2003 Spectra of the very large anisotropic scales in turbulent channels. *Phys. Fluids* **15** (6), 41–44.
- DEL ÁLAMO, J. C. & JIMÉNEZ, J. 2006 Linear energy amplification in turbulent channels. *J. Fluid Mech.* **559**, 205–213.
- DEL ÁLAMO, J. C. & JIMÉNEZ, J. 2009 Estimation of turbulent convection velocities and corrections to Taylor’s approximation. *J. Fluid Mech.* **640**, 5–26.
- DEL ÁLAMO, J. C., JIMÉNEZ, J., ZANDONADE, P. & MOSER, R. D. 2006 Self-similar vortex clusters in the turbulent logarithmic region. *J. Fluid Mech.* **561**, 329–358.
- ALIZARD, F. 2015 Linear stability of optimal streaks in the log-layer of turbulent channel flows. *Phys. Fluids* **27** (10), 105103.
- ANDERSSON, P., BRANDT, L., BOTTARO, A. & HENNINGSON, D. S. 2001 On the breakdown of boundary layer streaks. *J. Fluid Mech.* **428**, 29–60.
- BALTZER, J. R., ADRIAN, R. J. & WU, X. 2013 Structural organization of large and very large scales in turbulent pipe flow simulation. *J. Fluid Mech.* **720**, 236–279.
- BLACKWELDER, R. F. & ECKELMANN, H. 1979 Streamwise vortices associated with the bursting phenomenon. *J. Fluid Mech.* **94**, 577–594.
- BUTLER, K. M. & FARRELL, B. F. 1993 Optimal perturbations and streak spacing in wall-bounded turbulent shear flow. *Phys. Fluids* **3** (5), 774–777.
- CANTON, J., ÖRLÜ, R., CHIN, C. & SCHLATTER, P. 2016 Reynolds number dependence of large-scale friction control in turbulent channel flow. *Phys. Rev. Fluids* **1** (8), 081501.
- CASSINELLI, A., DE GIOVANETTI, M. & HWANG, Y. 2017 Streak instability in near-wall turbulence revisited. *J. Turbul.* **18** (5), 443–464.
- CHERNYSHENKO, S. I. & BAIG, M. F. 2005 The mechanism of streak formation in near-wall turbulence. *J. Fluid Mech.* **544**, 99–131.
- COSSU, C., PUJALS, G. & DEPARDON, S. 2009 Optimal transient growth and very largescale structures in turbulent boundary layers. *J. Fluid Mech.* **619**, 79–94.
- FLORES, O. & JIMÉNEZ, J. 2006 Effect of wall-boundary disturbances on turbulent channel flows. *J. Fluid Mech.* **566**, 357–376.
- FLORES, O. & JIMÉNEZ, J. 2010 Hierarchy of minimal flow units in the logarithmic layer. *Phys. Fluids* **22** (7), 1–4.
- DE GIOVANETTI, M., HWANG, Y. & CHOI, H. 2016 Skin-friction generation by attached eddies in turbulent channel flow. *J. Fluid Mech.* **808**, 511–538.
- HAMILTON, J. M., KIM, J. & WALEFFE, F. 1995 Regeneration mechanisms of near-wall turbulence structures. *J. Fluid Mech.* **287**, 317–348.
- HELLSTRÖM, L. H. O., MARUSIC, I. & SMITS, A. J. 2016 Self-similarity of the large-scale motions in turbulent pipe flow. *J. Fluid Mech.* **792**, R1 1–12.
- HOEPFFNER, J., BRANDT, L. & HENNINGSON, D. S. 2005 Transient growth on boundary layer streaks. *J. Fluid Mech.* **537**, 91–100.
- HOYAS, S. & JIMÉNEZ, J. 2006 Scaling of the velocity fluctuations in turbulent channels up to $Re_{\lambda} \approx 2003$. *Phys. Fluids* **18**, 1–4.
- HUTCHINS, N. & MARUSIC, I. 2007 Large-scale influences in near-wall turbulence. *Philos. Trans. R. Soc. A Math. Phys. Eng. Sci.* **365** (1852), 647–664.
- HWANG, Y. 2013 Near-wall turbulent fluctuations in the absence of wide outer motions. *J. Fluid Mech.* **723**, 264–288.
- HWANG, Y. 2015 Statistical structure of self-sustaining attached eddies in turbulent channel flow. *J. Fluid Mech.* **767**, 254–289.

- HWANG, Y. 2016 Mesolayer of attached eddies in turbulent channel flows. *Phys. Rev. Fluids* **1** (064401).
- HWANG, Y. & BENGANA, Y. 2016 Self-sustaining process of minimal attached eddies in turbulent channel flow. *J. Fluid Mech.* **795**, 708–738.
- HWANG, Y. & COSSU, C. 2010a Amplification of coherent streaks in the turbulent Couette flow: an input-output analysis at low Reynolds number. *J. Fluid Mech.* **643**, 333–348.
- HWANG, Y. & COSSU, C. 2010b Linear non-normal energy amplification of harmonic and stochastic forcing in the turbulent channel flow. *J. Fluid Mech.* **664**, 51–73.
- HWANG, Y. & COSSU, C. 2010c Self-sustained process at large scales in turbulent channel flow. *Phys. Rev. Lett.* **105** (4), 1–10.
- HWANG, Y. & COSSU, C. 2011 Self-sustained processes in the logarithmic layer of turbulent channel flows. *Phys. Fluids* **23** (6), 061702.
- HWANG, Y., WILLIS, A. P. & COSSU, C. 2016 Invariant solutions of minimal large-scale structures in turbulent channel flow for Re up to 1000. *J. Fluid Mech.* **802**, R1.
- JEONG, J. & HUSSAIN, F. 1997 Coherent structures near the wall in a turbulent channel flow. *J. Fluid Mech.* **332**, 185–214.
- JIMÉNEZ, J. 2013a How linear is wall-bounded turbulence? *Phys. Fluids* **25** (11).
- JIMÉNEZ, J. 2013b Near-wall turbulence. *Phys. Fluids* **25** (10), 101302.
- JIMÉNEZ, J. & HOYAS, S. 2008 Turbulent fluctuations above the buffer layer of wall-bounded flows. *J. Fluid Mech.* **611**, 215–236.
- JIMÉNEZ, J. & PINELLI, A. 1999 The autonomous cycle of near-wall turbulence. *J. Fluid Mech.* **389**, 335–359.
- JOVANOVIĆ, M. R., SCHMID, P. J. & NICHOLS, J. W. 2014 Sparsity-promoting dynamic mode decomposition. *Phys. Fluids* **26** (2), 1–22.
- KIM, H. T., KLINE, S. J. & REYNOLDS, W. C. 1971 The production of turbulence near a smooth wall in a turbulent boundary layer. *J. Fluid Mech.* **50** (1), 133–160.
- KIM, J. 2011 Physics and control of wall turbulence for drag reduction. *Philos. Trans. R. Soc. A Math. Phys. Eng. Sci.* **369** (1940), 1396–411.
- KIM, J., MOIN, P. & MOSER, R. D. 1987 Turbulence statistics in fully developed channel flow at low Reynolds number. *J. Fluid Mech.* **177**, 133–166.
- KIM, K. C. & ADRIAN, R. J. 1999 Very large-scale motion in the outer layer. *Phys. Fluids* **11** (2), 417–422.
- KLINE, S. J., REYNOLDS, W. C., SCHRAUB, F. A. & RUNDSTATLER, P. W. 1967 The structure of turbulent boundary layers. *J. Fluid Mech.* **30**, 741–773.
- KOVASZNAY, L. S. G. 1970 The Turbulent Boundary Layer. *Annu. Rev. Fluid Mech.* **2**, 95–112.
- LANDAHL, M. T. 1980 A note on an algebraic instability of inviscid parallel shear flows. *J. Comput. Phys.* **98**, 243–251.
- MARUSIC, I., MONTY, J. P., HULTMARK, M. & SMITS, A. J. 2013 On the logarithmic region in wall turbulence. *J. Fluid Mech.* **716**, R3 1–11.
- MONTY, J. P., HUTCHINS, N., NG, H. C. H., MARUSIC, I. & CHONG, M. S. 2009 A comparison of turbulent pipe, channel and boundary layer flows. *J. Fluid Mech.* **632**, 431–442.
- NICKELS, T. B., MARUSIC, I., HAFEZ, S. & CHONG, M. S. 2005 Evidence of the k^{-1} law in a high-Reynolds-number turbulent boundary layer. *Phys. Rev. Lett.* **95** (7), 1–4.
- PARK, D. S. & HUERRE, P. 1995 Primary and secondary instabilities of the asymptotic suction boundary layer on a curved plate. *J. Fluid Mech.* **283**, 249–272.
- PARK, J., HWANG, Y. & COSSU, C. 2011 On the stability of large-scale streaks in turbulent Couette and Poiseuille flows. *Comptes Rendus Mec.* **339** (1), 1–5.
- PERRY, A. E. & CHONG, M. S. 1982 On the mechanism of wall turbulence. *J. Fluid Mech.* **119**, 173–217.
- PERRY, A. E., HENBEST, S. & CHONG, M. S. 1986 Theoretical and experimental study of wall turbulence. *J. Fluid Mech.* **165**, 163–199.
- PERRY, A. E. & MARUSIC, I. 1995 A wall-wake model for the turbulence structure of boundary layers. Part 1. Extension of the attached eddy hypothesis. *J. Fluid Mech.* **298**, 389–407.
- PUJALS, G., GARCÍA-VILLALBA, M., COSSU, C. & DEPARDON, S. 2009 A note on optimal transient growth in turbulent channel flows. *Phys. Fluids* **21** (1), 1–6.
- REYNOLDS, W. C. & HUSSAIN, A. K. M. F. 1972 The mechanics of an organized wave in

- turbulent shear flow. Part 3. Theoretical models and comparisons with experiments. *J. Fluid Mech.* **54** (2), 263–288.
- REYNOLDS, W. C. & TIEDERMAN, W. G. 1967 Stability of turbulent channel flow, with application to Malkus's theory. *J. Fluid Mech.* **27** (2), 253–272.
- SCHMID, P. J. 2010 Dynamic mode decomposition of numerical and experimental data. *J. Fluid Mech.* **656**, 5–28.
- SCHMID, P. J. & HENNINGSON, D. S. 2001 *Stability and Transition in Shear Flows*. Springer.
- SCHOPPA, W. & HUSSAIN, F. 1998 Genesis of longitudinal vortices in near-wall turbulence. *Meccanica* **33** (5), 489–501.
- SCHOPPA, W. & HUSSAIN, F. 2002 Coherent structure generation in near-wall turbulence. *J. Fluid Mech.* **453**, 57–108.
- SHARMA, A. S. & MCKEON, B. J. 2013 On coherent structure in wall turbulence. *J. Fluid Mech.* **728**, 196–238.
- SMITH, C. R. & METZLER, S. P. 1983 The characteristics of low-speed streaks in the near-wall region of a turbulent boundary layer. *J. Fluid Mech.* **129**, 27–54.
- TOMKINS, C. D. & ADRIAN, R. J. 2003 Spanwise structure and scale growth in turbulent boundary layers. *J. Fluid Mech.* **490**, 37–74.
- TOWNSEND, A. A. 1961 Equilibrium layers and wall turbulence. *J. Fluid Mech.* **12**, 97–120.
- TOWNSEND, A. A. 1976 *The structure of turbulent shear flow*, 1st edn. Cambridge University Press.
- VREMAN, A. W. 2004 An eddy-viscosity subgrid-scale model for turbulent shear flow: Algebraic theory and applications. *Phys. Fluids* **16** (10), 3670–3681.
- WALEFFE, F. 1997 On a self-sustaining process in shear flows. *Phys. Fluids* **9** (4), 883–900.
- WILLIS, A. P., HWANG, Y. & COSSU, C. 2010 Optimally amplified large-scale streaks and drag reduction in turbulent pipe flow. *Phys. Rev. E* **82** (3), 1–11.
- ZARE, A., JOVANOVIĆ, M. R. & GEORGIU, T. 2017 Colour of turbulence. *J. Fluid Mech.* **812**, 636–680.
- ZHOU, J., ADRIAN, R. J., BALACHANDAR, S. & KENDALL, T. M. 1999 Mechanisms for generating coherent packets of hairpin vortices in channel flow. *J. Fluid Mech.* **387**, 353–396.